













A detailed time-resolved and energy-resolved spectro-polarimetric study of bright GRBs detected by *AstroSat* CZTI in its first year of operation

RAHUL GUPTA ^{1,2,3} S. B. PANDEY,³ S. GUPTA ^{4,5} T. CHATTOPADHAYAY ⁶ D. BHATTACHARYA ⁷
V. BHALERAO ⁸ A. J. CASTRO-TIRADO ^{9,10} A. VALEEV,¹¹ A. K. ROR ³ V. SHARMA ^{1,12,13} J. RACUSIN ¹,
A. ARYAN ^{3,14} S. IYYANI ¹⁵ AND S. VADAWALE ¹⁶

¹*Astrophysics Science Division, NASA Goddard Space Flight Center, Mail Code 661, Greenbelt, MD 20771, USA*

²*NASA Postdoctoral Program Fellow*

³*Aryabhata Research Institute of Observational Sciences (ARIES), Manora Peak, Nainital-263002, India*

⁴*Bhabha Atomic Research Center, Mumbai, Maharashtra-400094, India*

⁵*Homi Bhabha National Institute, Mumbai, Maharashtra-400094, India*

⁶*Kavli Institute of Particle Astrophysics and Cosmology, Stanford University, 452 Lomita Mall, Stanford, CA 94305, USA*

⁷*Department of Physics, Ashoka University, Sonapat, Haryana-131029, India*

⁸*Indian Institute of Technology Bombay Powai, Mumbai, Maharashtra 400076, India*

⁹*Instituto de Astrofísica de Andalucía (IAA-CSIC), Glorieta de la Astronomía s/n, E-18008, Granada, Spain*

¹⁰*Departamento de Ingeniería de Sistemas y Automática, Escuela de Ingenierías, Universidad de Málaga, C. Dr. Ortiz Ramos sn, E-29071, Málaga, Spain*

¹¹*Special Astrophysical Observatory of Russian Academy of Sciences, Nizhniy Arkhyz, Russia*

¹²*University of Maryland, Baltimore County, Baltimore, MD 21250, USA*

¹³*Center for Research and Exploration in Space Science and Technology, NASA/GSFC, Greenbelt, MD 20771, USA*

¹⁴*Graduate Institute of Astronomy, National Central University, 300 Jhongda Road, 32001 Jhongli, Taiwan*

¹⁵*Indian Institute of Science Education and Research, Thiruvananthapuram, Kerala, India, 695551*

¹⁶*Physical Research Laboratory Thaltej, Ahmedabad, Gujarat 380009, India*

(Received May 5, 2024; Revised June 14, 2024; Accepted June 21, 2024)

ABSTRACT

The radiation mechanism underlying the prompt emission remains unresolved and can be resolved using a systematic and uniform time-resolved spectro-polarimetric study. In this paper, we investigated the spectral, temporal, and polarimetric characteristics of five bright GRBs using archival data from *AstroSat* CZTI, *Swift* BAT, and *Fermi* GBM. These bright GRBs were detected by CZTI in its first year of operation, and their average polarization characteristics have been published in [Chattopadhyay et al. \(2022\)](#). In the present work, we examined the time-resolved (in 100-600 keV) and energy-resolved polarization measurements of these GRBs with an improved polarimetric technique such as increasing the effective area and bandwidth (by using data from low-gain pixels), using an improved event selection logic to reduce noise in the double events and extend the spectral bandwidth. In addition, we also separately carried out detailed time-resolved spectral analyses of these GRBs using empirical and physical synchrotron models. By these improved time-resolved and energy-resolved spectral and polarimetric studies (not fully coupled spectro-polarimetric fitting), we could pin down the elusive prompt emission mechanism of these GRBs. Our spectro-polarimetric analysis reveals that GRB 160623A, GRB 160703A, and GRB 160821A have Poynting flux-dominated jets. On the other hand, GRB 160325A and GRB 160802A have baryonic-dominated jets with mild magnetization. Furthermore, we observe a rapid change in polarization angle by ~ 90 degrees within the main pulse of very bright GRB 160821A, consistent with our previous results. Our study suggests that the jet composition of GRBs may exhibit a wide range of magnetization, which can be revealed by utilizing spectro-polarimetric investigations of the bright GRBs.

Corresponding author: Rahul Gupta

rahulbhu.c157@gmail.com,
shashi@aries.res.in

rahul.gupta@nasa.gov,

Keywords: gamma-ray burst: general, methods: data analysis, polarization, radiation mechanism

1. INTRODUCTION

Gamma-ray bursts (GRBs) are among the most energetic and enigmatic phenomena in the Universe. They emit an immense amount of energy in the form of high-energy photons occurring during cataclysmic events such as the collapse of massive stars or the merging of compact objects (Piran 2004; Kumar & Zhang 2015). The exact radiation mechanism driving the prompt emission remains elusive (Baring & Braby 2004; Zhang 2011; Bošnjak et al. 2022). Synchrotron emission, typically associated with the radiation emitted as relativistic electrons accelerated in magnetic fields, is commonly believed to underlie the spectral shape of the prompt emission (Uhm & Zhang 2014; Oganessian et al. 2019; Tavani 1996; Zhang 2020). The low energy spectral slope (α_{pt}) acts as an indicator tool for understanding the potential radiation physics of GRBs. In scenarios involving fast cooling synchrotron emission, where relativistic electrons rapidly emit all their energy upon acceleration, the theoretically predicted value of α_{pt} is $-3/2$ (Granot et al. 2000). However, upon examining the distribution of α_{pt} for numerous GRBs observed with various telescopes such as *CGRO*/BATSE and *Fermi*/GBM, it becomes clear that a substantial number of bursts do not align with the expected characteristics of synchrotron emission (Preece et al. 1998). This inconsistency suggests the involvement of alternative mechanisms in generating some or all of the emissions. For instance, physical models of photospheric emission have been observed to directly fit the observational data (Pe’Er & Ryde 2017; Beloborodov & Mészáros 2017; Acuner et al. 2020; Fan et al. 2012). Moreover, thermal photospheric spectra need not strictly adhere to a `Blackbody` distribution; if dissipation takes place just beneath the photosphere, this process could widen the spectrum compared to the standard `Blackbody` spectrum (Beloborodov 2017; Ahlgren et al. 2019; Rees & Mészáros 2005; Ryde et al. 2011). Additionally, non-dissipative broadening of the photospheric emission can occur due to high latitude emission, often referred to as the multi-color `Blackbody` effect (Lundman et al. 2013; Pe’er 2015; Acuner et al. 2019). This effect arises because different parts of the photosphere can have different temperatures, leading to a spectrum that is broader than a single `Blackbody`.

In recent years, significant strides have been made in the study of radiation physics through broadband spectroscopy of prompt emissions. Oganessian et al. (2017, 2018) performed a joint spectral analysis on a sample of 34 bright bursts observed concurrently by the

Swift Burst Alert Telescope (BAT) and the X-ray Telescope (XRT), focusing on prompt gamma-ray emissions. This analysis identified a distinct lower frequency energy break in addition to the typical peak energy break. Notably, the values for α_1 (photon index below the low energy break) and α_2 (photon index above the low energy break) aligned with synchrotron theory predictions. This spectral behavior was similarly noted in bright long GRBs observed by *Fermi*, as discussed by Ravasio et al. (2018, 2019), though it was not present in bright short GRBs from *Fermi*. We also noted comparable spectral characteristics in one of the brightest long-duration GRBs detected by *Fermi* (GRB 190530A, Gupta et al. 2022a; Gupta 2023). Furthermore, Oganessian et al. (2019) expanded the analysis to include the optical band and concluded that the synchrotron spectral shape fits well across the spectrum from gamma-ray to optical bands, using a synchrotron physical model. However, it is important to note that the resulting parameters of the spectral fits, such as the bulk Lorentz factor, number density of electrons, and magnetic field strength, showed inconsistencies compared to other GRB prompt emissions analyses. These discrepancies highlight the complexities involved in modeling the emission region of the jet and suggest the need for further investigation to reconcile these differences. These findings further highlight the potential of simultaneous multi-band observations of prompt emissions, from optical to GeV energies, to deepen our understanding of emission mechanisms. However, capturing such simultaneous observations remains a significant challenge due to the extremely short and variable nature of prompt emissions, often concluding before there is time to redirect optical/X-ray instruments to the burst location (Gupta 2023).

Currently, a major challenge in the spectral analysis of GRBs is the degeneracy among various spectral models. Often, the same dataset can be effectively fitted with different spectral models, all yielding comparably good statistical results (Iyyani et al. 2016). The spectroscopic study of prompt gamma-ray emission of GRBs provides valuable information, yet it alone is inadequate to fully discriminate between various emission models. Consequently, there is a critical need for more constraining observables, such as polarization, for example. (Iyyani 2022; Toma 2013; Gill et al. 2020).

Polarization measurements offer a reliable means of distinguishing between various potential radiation models of GRBs. This is because different models for prompt emission radiation predict distinct polarization fractions

depending on the geometry of the jet. Typically, any asymmetry in the emitting region or viewing geometry results in linearly polarized emission. Synchrotron radiation originating from structured magnetic fields and observed along the jet axis is expected to exhibit a high degree of polarization. Conversely, inverse Compton and photospheric emission typically yield low polarization fractions, except when the jet is observed off-axis (Toma et al. 2009). Therefore, by conducting polarization measurements for numerous bursts, we can gain tangible insights into the emission mechanisms of GRBs. Therefore, combining polarization measurement with spectroscopy can effectively resolve the degeneracy among different spectral models. Additionally, variations in polarization are crucial as they influence the underlying emission mechanism (Gill et al. 2021; McConnell 2017). The temporal evolution of polarization also serves as a vital tool for comprehending the dynamic nature of the jet. Thus, time-resolved spectro-polarimetric measurements offer valuable information for distinguishing between different GRB models and understanding the radiation mechanisms involved.

Polarization measurements of prompt emission present significant challenges and have yet to be extensively conducted (Gill et al. 2021). As of now, such measurements have been attempted for only a limited number of bursts, approximately 40, utilizing instruments such as the Reuven Ramaty High Energy Solar Spectroscopic Imager (*RHESSI*; Coburn & Boggs 2003; Rutledge & Fox 2004), the BATSE Albedo Polarimetry System (BAPS; Willis et al. 2005), the INTERNATIONAL Gamma-Ray Astrophysics Laboratory (*INTEGRAL*; Kalemci et al. 2007; McGlynn et al. 2007), the GAMMA-ray burst Polarimeter (GAP; Yonetoku et al. 2011a,b, 2012), the Cadmium Zinc Telluride Imager onboard *AstroSat* and POLAR (Kole et al. 2020; Burgess et al. 2019). However, most analyses have focused only on time and energy-integrated polarization measurements (Chattopadhyay 2021).

Recently, we in Chattopadhyay et al. (2022) reported the first catalog of prompt emission polarization measurements, focusing on twenty bright GRBs observed by Cadmium Zinc Telluride Imager (CZTI) during its first five years of operation. These bursts were selected for their brightness to maximize the number of Compton events available for polarization analysis. The analysis revealed time-integrated polarization measurements in the energy range of 100–600 keV. Based on the time-integrated polarization analysis, we found that most of these bursts ($\sim 75\%$) exhibited a low or zero polarization in the full burst interval (time-resolved and energy-resolved polarization measurement is required to exam-

ine if they are intrinsically unpolarized or the polarization angle within the burst is changing over the time) and only about 25 % of the sample show indications of high linear polarization, including some as high as $71.43\% \pm 26.84\%$ (GRB 180103A). Such high polarization implies that the mechanism for prompt emission could either be synchrotron radiation within a time-independent ordered magnetic field or Compton drag.

On the other hand, the POLAR instrument was also designed to perform linear polarization measurements of GRBs within an energy range of approximately 50-500 keV. Kole et al. (2020) analyzed a sample of GRBs detected by POLAR and reported that the time-integrated analysis of the GRBs in their selection is compatible with a low or zero polarization Chattopadhyay et al. (2022) compared the GRB polarization measurements made by POLAR and *AstroSat*. POLAR, with an energy range of 50-500 keV, is sensitive to lower energies and samples with longer burst durations. In contrast, *AstroSat*, sensitive to energies above 100 keV, samples shorter burst durations. GRB emissions are typically highly structured, and several GRBs, such as GRB 160821A (Sharma et al. 2019), GRB 170114A (Burgess et al. 2019), and GRB 100826A (Yonetoku et al. 2011a), have shown polarization angle changes during bursts. Thus, POLAR’s longer sampling duration makes it more likely to detect emissions with varying polarization angles, resulting in lower polarization observations compared to *AstroSat*’s higher energy, shorter duration sampling. In addition, the discrepancies could also arise from instrument systematics or differences in the GRBs observed by each instrument.

In this paper, we performed the time-resolved and energy-resolved polarization measurements of five bright bursts observed by CZTI in its first year of operation to verify whether the polarization properties are changing for these bursts. Additionally, we also performed a comprehensive time-resolved spectral analysis of those bursts observed by the *Fermi* mission to constrain their radiation physics. The paper’s layout is as follows: In § 2, we have given the details about our sample for the present study. In § 3, we have given the methods of time-averaged, time-resolved, and energy-resolved spectro-polarimetric data analysis. The results and discussion of this work are given in § 4 and in § 5, respectively. Finally, we have given a summary & conclusion of this work in § 6.

2. SAMPLE SELECTION AND PREVIOUS POLARIZATION MEASUREMENTS

For the present work, we selected five GRBs (GRB 160325A, GRB 160623A, GRB 160703A, GRB 160802A,

Table 1. List of bright gamma-ray bursts and their properties under investigation in our sample. The reported values of time-integrated polarization fractions (PF) obtained from [Chattopadhyay et al. \(2022\)](#) are listed in the last column. *AstroSat* orbit IDs cited here correspond to those in which the necessary data were telemetered to the ground station. The data include those of Target of Opportunity (ToO), Announcement of Opportunity (AO), and Guaranteed Time (GT) observations. The redshift measurement/host search for the sample was attempted utilizing larger telescopes, such as the 10.4m GTC and the 3.6m DOT (4K \times 4K IMAGER and TANSPEC) to study such transients ([Pandey 2016](#)).

Sr. No.	GRB name	Redshift/Host limit (mag)	T_{90}	<i>AstroSat</i> Orbit ID	Compton Counts	Time-integrated PF (%)
1	GRB 160325A	–	42.94 ± 0.57	2652	764	< 45.02
2	GRB 160623A	0.367	107.78 ± 8.69	3983	1714	< 56.51
3	GRB 160703A	< 1.5/> 23 (i)	44.40 ± 2.80	4135	433	< 62.64
4	GRB 160802A	–	16.38 ± 0.36	4576	1511	< 51.89
5	GRB 160821A	> 23.6 (R)	43.01 ± 0.72	4866	2851	< 33.87

and GRB 160821A) to investigate in-depth the time-resolved and energy-resolved spectral and polarimetric characteristics. These bright bursts were observed by *AstroSat* in its first year of operation. These GRBs are selected based on their brightness (fluence values greater than 10^{-5} erg cm $^{-2}$) and their detection in CZTI within certain angles (0-60 and 120-180), where CZTI has good sensitivity for polarization measurements (see section 2 of [Chattopadhyay et al. 2022](#) for more information about sample selection). The selected sample of bright bursts (see Figure 1) for this study and their time-integrated polarization have been tabulated in Table 1. Below, we provide brief observations of individual bursts and their previous polarization measurements.

2.1. GRB 160325A

GRB 160325A was triggered by *Fermi* GBM ([Meegan et al. 2009](#)) and LAT ([Atwood et al. 2009](#)) simultaneously at 06:59:21.51 UT on March 25, 2016 ([Roberts 2016](#); [Axelsson et al. 2016](#)). The GBM light curve of GRB 160325A has two separate emission episodes with a total T_{90} duration of 43 sec in 50 -300 keV. The gamma-ray/hard X-ray instruments like *Swift* BAT ([Barthelmy et al. 2005](#); [Sonbas et al. 2016](#)), *Konus-Wind* ([Tsvetkova et al. 2016](#)), and *AstroSat* ([Chattopadhyay et al. 2019](#)) also detected GRB 160325A. Previously, we studied the spectro-polarimetric properties of individual episodes of GRB 160325A and noted that both episodes have different spectral and polarimetric properties. The first episode of GRB 160325A is best fitted using **Cutoff power-law + Blackbody** function and has a low polarization fraction (< 37 %, an upper limit in 100-380 keV), suggesting sub-photospheric model as a dominant radiation model for this episode. On the other hand, the second episode of GRB 160325A is best fitted using **Cutoff power-law** function and has high polarization fraction (> 43 %, a lower limit in 100-380 keV), suggesting thin shell synchrotron radiation model ([Sharma et al. 2020](#)). Our joint spectro-polarimetric analysis in-

dicates a change in the spectral and polarimetric properties of two episodes of GRB 160325A.

2.2. GRB 160623A

GRB 160623A was detected by *Fermi* GBM at 05:00:34.23 UT on June 23, 2016, ([Mailyan et al. 2016](#)). GRB 160623A was also detected by other GRB triggering instruments *Konus-Wind* ([Frederiks et al. 2016a](#)), CALET Gamma-Ray Burst Monitor ([Yamaoka et al. 2016](#)), *Fermi* LAT ([Vianello et al. 2016](#)), and *AstroSat* ([Chattopadhyay et al. 2019](#)). We noted that *Konus-Wind*, CALET, and *AstroSat* detected a bright emission pulse followed by weaker emission phases. However, GBM could not detect the brighter main emission pulse due to the Earth’s occultation of the source. GBM detected weaker emission of around 50 sec (see Figure A2 of the appendix). Recently, we reported the time-averaged PF of (< 56.51 %, an upper limit) in 100-600 keV using *AstroSat*/CZTI observations ([Chattopadhyay et al. 2022](#)).

For this burst, *Swift* XRT discovered X-ray afterglow and also observed bright dust-scattered features (radius \sim 3.5 arcmin) around this GRB ([Mingo et al. 2016](#); [Tiengo et al. 2016](#); [Pintore et al. 2017](#)). Many ground-based facilities detected the optical/mm/radio afterglows of GRB 160623A.

Utilizing the precise localization of the optical afterglow of GRB 160623A, [Malesani et al. \(2016\)](#) reported the spectroscopic redshift of the burst ($z = 0.367$). We also conducted observations of the optical afterglow of GRB 160623A using the 10.4m Gran Telescopio Canarias (GTC) as a part of a larger collaboration. Spectra were gathered at various epochs: on June 25 (1.9 days post-burst) and July 3/4, 2016. We utilized both the R1000B and R2500I grisms, covering the wavelength range of 3800-10000 Å. Analysis of the reddest spectrum (2 x 1200 sec with R2500I) at the afterglow position revealed emission lines of H-alpha and [SII], enabling us to determine a redshift of $z = 0.367$ (see Figure A1 of the

appendix), which corroborates the value proposed by Malesani et al. (2016). Additionally, the bluest range spectrum (1200 sec) indicated a marginal detection of H-beta, considering the high foreground Galactic extinction along the line of sight. The faint continuum observed in the spectrum from the first epoch extended down to 3800 Å, with no discernible absorption lines present. Based on these observations, we confirmed that this redshift corresponds to the host galaxy of GRB 160623A (Castro-Tirado et al. 2016).

2.3. GRB 160703A

GRB 160703A was detected by *Swift* BAT at 12:10:05 UT on July 03, 2016 with a T_{90} duration of 44.4 ± 2.8 sec (Cenko et al. 2016; Lien et al. 2016). The prompt emission of GRB 160703A was also observed by *Konus-Wind* (Frederiks et al. 2016b) and *AstroSat* (Bhalerao et al. 2016a). Based on *AstroSat* CZTI observations of GRB 160703A, we reported the high value of time-averaged PF (< 62.64 %, an upper limit) in 100-600 keV (Chattopadhyay et al. 2022).

The X-ray and optical counterpart of GRB 160703A was detected by *Swift* XRT and UVOT instruments (D’Elia et al. 2016; Hagen & Cenko 2016). The UVOT detected the afterglow of GRB 160703A in all its seven filters, based on this Hagen & Cenko (2016) constrained the redshift of the burst ($z < 1.5$). Later follow-up observations using the Giant Metrewave Radio Telescope (GMRT) telescope detected a faint potential radio counterpart of GRB 160703A (Nayana et al. 2016).

2.4. GRB 160802A

At 06:13:29.63 UT on August 02, 2016, GRB 160802A was triggered by *Fermi* GBM with T_{90} of 16.4 sec (in 50-300 keV). GBM provides the localization as RA= 35.29, DEC = +72.69 (J2000) with uncertainty radius of 1 degree (Bissaldi 2016). The GBM light curve of GRB 160802A has two clearly separated emission episodes (see Figure A2 of the appendix). GRB 160802A was one of the brightest (energy fluence 1.04×10^{-4} erg s^{-2} in 10-1000 keV) *Fermi* GBM detected bursts. The burst was independently detected by other gamma-ray detecting satellites/instruments such as *AstroSat* CZTI (Bhalerao et al. 2016b), *Konus-Wind* (Kozlova et al. 2016a), Lomonosov BDRG (Panasyuk et al. 2016), and CALET Gamma-ray Burst Monitor (Tamura et al. 2016).

We in Chand et al. (2018) studied the spectro-polarimetric study of GRB 160802A using joint *Fermi* and *AstroSat* observations. We performed spectral analysis using empirical functions and XSPEC software. We noted that the evolution of low-energy photon indices

of the **Band** function is harder than those theoretically expected from thin shell synchrotron slow and fast cooling model, indicating photospheric origin. Additionally, we calculated the time-averaged PF = 85 ± 29 % using previous polarization tools in 100-300 keV (Chand et al. 2018). A high value of the time-averaged PF (< 51.89 %, an upper limit) was also measured 100-600 keV in Chattopadhyay et al. (2022) for GRB 160802A using improved polarimetric techniques. Such a high value of PF indicates a synchrotron model if the source was observed on-axis. On the other hand, the photospheric model can also produce such high PF if the source is viewed along the edge. Based on our joint *Fermi* and *AstroSat* spectro-polarimetric observations, we suggested that GRB 160802A might have originated due to sub-photospheric dissipation viewed along the edge (Chand et al. 2018).

2.5. GRB 160821A

GRB 160821A was detected by *Swift* BAT and *Fermi* GBM at 20:34:30 UT on 21 August 2016 (Siegel et al. 2016; Stanbro & Meegan 2016). The prompt emission of the burst was also discovered independently using *Fermi* LAT (McEnery et al. 2016), *Konus-Wind* (Kozlova et al. 2016b), CALET (Marrocchesi et al. 2016), and *AstroSat* (Bhalerao et al. 2016c). The burst is extremely bright which provides a unique opportunity for detailed spectro-polarimetric analysis using *Fermi-AstroSat* observations. We performed the spectro-polarimetric analysis of GRB 160821A and noted a high PF (66_{-27}^{+26} %) in the time-averaged polarization measurements (in 100-300 keV). Additionally, the time-resolved polarization measurements give evidence of a change in polarization angle by twice during the entire emission phase of GRB 160821A (Sharma et al. 2019). Recently, for this burst, we reported the time-averaged PF (< 33.87 %, an upper limit) in 100-600 keV utilizing the improved polarization measurement tools (Chattopadhyay et al. 2022).

3. DATA ANALYSIS

We utilized *AstroSat* CZTI data for the polarization measurements of the GRBs in our sample, while *Fermi* and *Swift* observations were employed for the spectral analysis of the bursts (see details below). It is crucial to clarify that our analysis does not involve a fully coupled spectro-polarimetric fitting. Despite the absence of a fully coupled spectro-polarimetric analysis, our study provides significant insights into the polarization characteristics and emission mechanisms of the GRBs under investigation.

3.1. Technique of polarization analysis and improvements

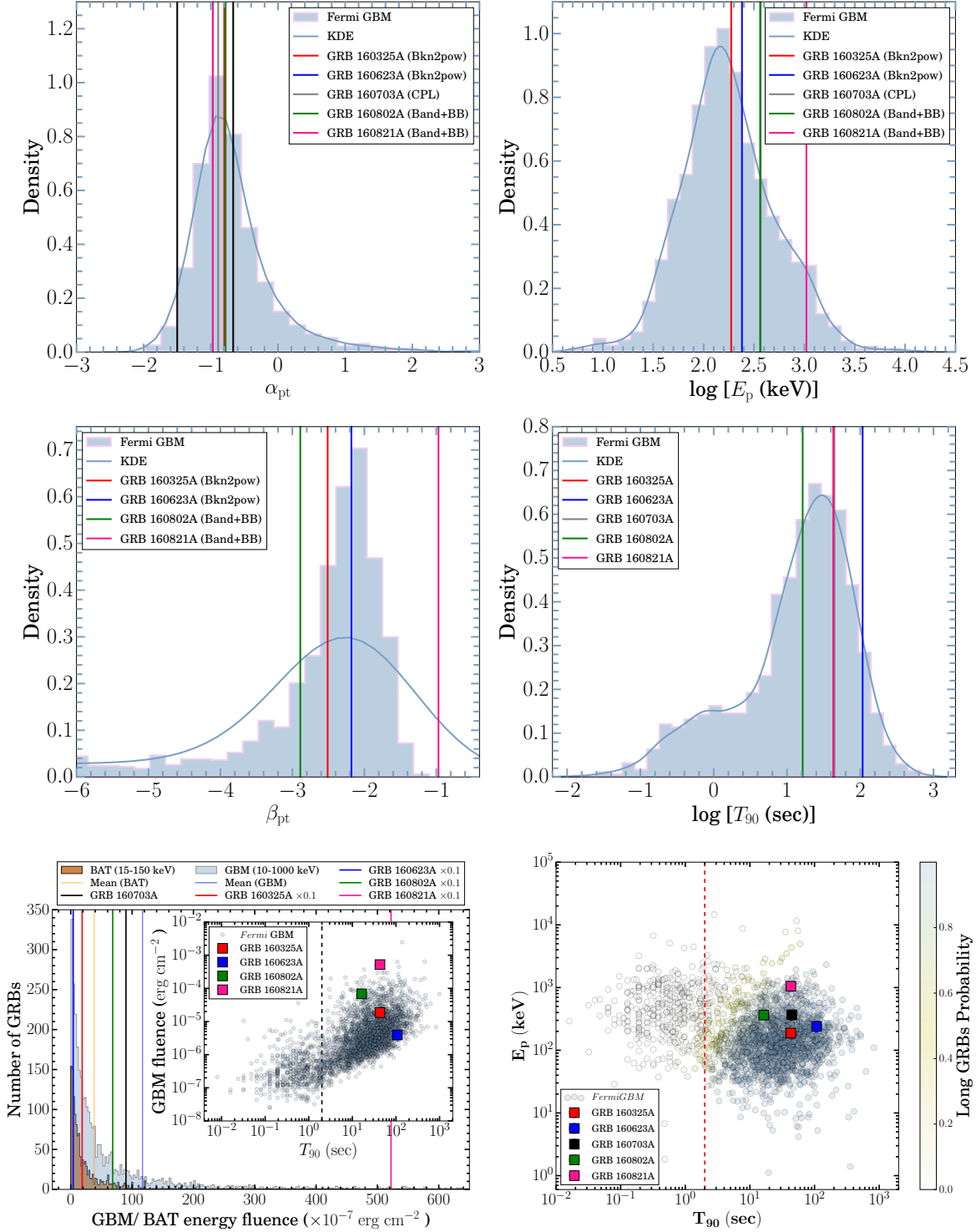


Figure 1. Prompt emission characteristic of the GRBs: The distributions of basic spectral (α_{pt} (top-left), E_p (top-right), β_{pt} (middle-left)) and temporal (T_{90} , middle-right) properties of GBM detected GRBs. The solid black lines correspond to the theoretically predicted values of the low energy photon index from thin-shell synchrotron emission models. The vertical colored lines denote the position of GRBs under study in this paper. The Kernel density estimations (KDE) for all the distributions are shown using grey curves. Bottom-left: Histogram of *Fermi* GBM (light blue) and *Swift* BAT (orange) energy fluence values. The mean fluence values for the BAT and GBM samples are marked by vertical solid orange and blue lines, respectively. The positions of all five bursts in our sample are marked using vertical-colored lines. The inset plot illustrates the relationship between energy fluence and duration for *Fermi* GRBs. Bottom-right: E_p - T_{90} (harness-duration) plot for *Fermi* GBM GRBs. The location of five GRBs in our sample is shown using colored squares. The vertical red line represents the threshold for classifying bursts. The figure displays the long and short bursts obtained from the GBM catalog. The probability of long GRBs is represented on the right side of the Y-scale.

The *AstroSat* CZTI mainly serves as a hard X-ray imaging/spectroscopy detector with a wide field of view. Notably, its ground calibration has revealed polarization measurement capabilities for on-axis sources. Recent experimentation by Vaishnava et al. (2022) has further validated CZTI’s ability to measure off-axis hard X-ray polarization for bright sources such as GRBs. Above 100 keV, CZTI exhibits a notable probability of Compton scattering. Leveraging the pixilated nature of CZT detectors, it functions as a Compton Polarimeter. Given its distinctive hard X-ray polarization measurement capabilities, the CZTI team has reported polarization measurements of both persistent (such as the Crab pulsar and nebula) and transient (including GRBs) X-ray sources (Rao et al. 2016; Vadawale et al. 2018; Chattopadhyay et al. 2019). Despite moderate brightness, energetic transient sources like GRBs are the potential hard X-ray for polarization measurements due to the simultaneous availability of pre and post-burst backgrounds with higher signal-to-noise ratios. For a comprehensive understanding of the prompt emission polarization analysis of GRBs using CZTI data, we in Chattopadhyay et al. (2022) present detailed techniques. In this study, we present a concise overview of the steps and recent enhancements in the polarization analysis tool for CZTI data.

- Selection of Compton events: To conduct polarization analysis using CZTI data, we initially chose double events detected within a 20 μ s temporal window. Subsequently, we applied Compton criteria, assessing the ratio of energies received on neighboring pixels, to filter out double events resulting from chance coincidence.
- Creation of Background-Subtracted Azimuthal Angle Distribution: Compton events were selected within both the GRB emission region and the pre- and post-burst background regions. To define the latter, we excluded instances of spacecraft crossing the South Atlantic Anomaly. Following this, we subtracted the raw azimuthal angle distribution of the GRB emission region from that of the background, resulting in the final background-subtracted azimuthal angle distribution for the GRB.
- Correction for geometric effects: Systematic errors stemming from geometric effects and off-axis detection of GRBs impact the background-subtracted azimuthal angle distribution. To address this, we employed the Geant4 toolkit and the *AstroSat* mass model to simulate an unpo-

larized azimuthal angle distribution. This simulation considered the distribution of photons observed from GRB spectra at the same orientation as the *AstroSat* spacecraft. Subsequently, we normalized the observed background-subtracted azimuthal angle distribution of the GRB using the simulated unpolarized azimuthal angle distribution.

- Calculation of Modulation Amplitude and Polarization Angle: We employed a sinusoidal function to fit the observed background-subtracted and geometry-corrected azimuthal angle distribution of the GRB. This fitting process enabled us to determine the modulation factor (μ) and polarization angle within the *AstroSat* CZTI plane. For the sinusoidal function fitting, we utilized the Markov chain Monte Carlo (MCMC) method.
- Calculation of Polarization Fraction: To ascertain the polarization fraction, normalization of the modulation factor (μ) with the simulated modulation amplitude for 100% polarized radiation μ_{100} is required. This value is obtained through Geant4 toolkit simulations using the *AstroSat* mass model for the same direction and observed spectral parameters. Subsequently, the PF is calculated by normalizing μ with μ_{100} for those bursts exhibiting a Bayes factor greater than 2. In instances where the Bayes factor is below 2, we establish a constraint on the polarization fraction by setting a 2σ upper limit (refer to Chattopadhyay et al. 2022 for further details).

Furthermore, we have implemented the following enhancements in the polarization data analysis of the *AstroSat* CZTI for this study. This upgraded CZTI pipeline is being utilized for the first time for executing time and energy-resolved polarization measurements of bursts detected by the *AstroSat* CZTI.

3.1.1. Low gain pixels and energy bandwidth

Since the launch of the *AstroSat* mission, around 20% of the CZTI pixels were observed to have electronic gains lower (2–4 times) than the laboratory-tested gain values. In the previous studies (e.g., Chand et al. 2018; Chattopadhyay et al. 2019; Chand et al. 2019; Sharma et al. 2019, 2020; Gupta et al. 2022a), the sensitive spectroscopic and polarimetric information in 100 - 300 keV were extracted using the normal-gain pixels only. However, the electronic gain for the low-gain pixels has been constant since the first day of working of CZTI in space; therefore, considering the low-gain pixels after rigorous

calibration can extend the energy channels of Compton energy spectra and polarization up to 600 keV. This new characteristic also makes wider the spectral coverage using single-pixel up to the sub-MeV capacity (~ 1 MeV), earlier it was restricted to 150 keV (Chattopadhyay et al. 2021). Recently, we applied this method for the time-averaged polarization measurement of twenty GRBs detected by the *AstroSat* CZTI in its five years of operation (Chattopadhyay et al. 2022). We are now implementing these improvements for the first time in time-resolved and energy-resolved polarimetric measurements of bright bursts. This new methodology significantly enhances outcomes and extends the energy coverage for prompt emission spectro-polarimetric analysis.

3.1.2. New event selection logic

Hard X-ray detectors are typically sensitive to background noise, such as cosmic rays, owing to their non-focusing nature at these wavelengths. As a result, it is crucial to identify and eliminate such noise events, selecting only those unaffected by background interference for scientific analysis. In the case of CZTI, the previous analysis pipeline for time-resolved spectro-polarimetric studies has incorporated techniques for event selection, but these techniques have some constraints. For example, these algorithms were mainly developed to analyze data from regular X-ray sources where the object flux is significantly lower than the background and thus is not well equipped for transient events like GRBs. Ratheesh et al. (2021) re-investigated the features of noise events in CZTI and gave a generalized event choice technique that provides analysis for all types of sources, including GRBs. This algorithm significantly reduces noise levels without considering the source flux dependence. In our current study, focusing on time-resolved and energy-resolved polarimetric analysis using CZTI data, we have used this algorithm, leveraging its improved capability for noise reduction across various source types.

3.2. Technique of temporal and spectral analysis

The temporal profiles of GRBs exhibit distinct characteristics attributed to the erratic behavior of the central engine. To extract temporal information from *Fermi* GBM data, we employed the Fermi GBM Data Tools (Goldstein et al. 2022). Furthermore, to extract spectra from *Fermi* GBM data, we employed the `gtburst` tool¹. For BAT data, both temporal and spectral analyses were carried out using `HEASOFT`, utilizing the most recent BAT calibration files. For detailed insights into

the technique employed for BAT data analysis, refer to Gupta et al. (2021). It is important to note that `3ML` plugin for the simultaneous fitting of BAT data with data from other instruments, such as *Konus-Wind*, *AstroSat*, etc, is not currently available. Consequently, for GRBs observed with BAT, we have relied exclusively on the spectral parameters derived from the *Konus-Wind* instrument, as reported in Chattopadhyay et al. (2022). Below, we have provided details of our spectral analysis (empirical and physical synchrotron model). However, we did not explore the physical photospheric models due to the lack of a publicly available robust and validated photospheric model (compatible with `3ML`).

3.2.1. Empirical spectral modeling

For the prompt emission spectral modeling of GRBs, we employed the Multi-Mission Maximum Likelihood framework (Vianello et al. 2015, `3ML`). Typically, the GRB spectrum can be adequately described by an empirical `Band` function. Therefore, we initially fitted the spectrum of GRBs of our sample using `Band` function. Subsequently, we explored additional empirical functions such as power-law (PL), `Cutoff power-law` (CPL), and `bkn2pow`, considering model parameters and statistical measures/residuals from spectral fitting with `3ML`. The selection of the best-fit model was determined based on the difference in deviance information criterion (DIC) values obtained from various models. A comprehensive method for empirical spectral modeling is provided in Caballero-García et al. (2023).

3.2.2. Physical spectral modeling

Burgess et al. (2020) showed that empirical function could be fallacious, and we should use physical spectral modeling to constrain the radiation physics of prompt emission. Burgess et al. (2020) further showed that even if the low-energy index of `Band` function exceeds the line of death of the synchrotron model, the spectrum still could be fitted using physical thin shell synchrotron model. Additionally, due to the spectral curvature of empirical functions, the empirical spectral models may lead to incorrect interpretations of the radiation physics of GRBs. So, we have utilized the physical thin shell synchrotron model to accurately interpret the emission mechanism. For the present work, we have applied publicly available `pynchrotron`² physical model for the time-integrated and time-resolved spectral fitting of GBM data in `3ML` (Burgess et al. 2020). `pynchrotron` model executes the synchrotron emission from a cooling population of electrons in the thin shell

¹ <https://fermi.gsfc.nasa.gov/ssc/data/analysis/scitools/gtburst.html>

² <https://github.com/grburgess/pynchrotron>

case. According to the `pynchrotron` model, the relativistic electrons follow a power-law distribution $N(\gamma) \propto \gamma^{-p}$ with $\gamma_{inj} \leq \gamma \leq \gamma_{max}$. In this equation, p represents the power-law index of the energy distribution of injected electron, γ_{inj} represents the lower limit, and γ_{max} represents the upper limit of the relativistic electron spectrum. `pynchrotron` model consists of six model parameters: 1. the power-law index of the energy distribution of injected electron (p), 2. The strength of magnetic field (B), 3. γ_{max} , 4. γ_{inj} , 5. Bulk Lorentz factor (γ_{bulk}) of the relativistic jet, and 6. Lorentz factor for the electron cooling time scale (γ_{cool}). Although, while the physical spectral modeling of GRBs, we fixed the $\gamma_{inj} = 10^5$ (due to degeneracy between B and γ_{inj}), $\gamma_{max} = 10^8$ (slow cooling synchrotron model better fit the prompt spectrum). Additionally, we have also fixed the γ_{bulk} for GRBs utilizing the prompt emission correlation between γ_{bulk} and isotropic gamma-ray energy.

3.3. Search for potential host galaxies using DOT

The expected polarization fraction from different radiation models depends on the jet viewing geometry, and this can be further verified by investigating the $\Gamma\theta_j$ condition, where Γ represents the bulk Lorentz factor and θ_j denotes the jet opening angle (see section 5.1 for more information). Γ and θ_j could be calculated using the Liang relation (the correlation between isotropic gamma-ray energy and Γ , Liang et al. 2010) and the jet breaks observed in the afterglow light curve, respectively. However, both of these parameters depend on the redshift. Therefore, redshift is a very important parameter to verify the $\Gamma\theta_j$ condition and predict the possible radiation mechanism based on the observed value of polarization fraction. We observed that only two GRBs (GRB 160623A and GRB 160703A) in our sample have redshift constraints. No redshift measurements were found in the literature for the remaining GRBs. To determine their photometric redshift, we attempted to locate the associated host galaxies of the bursts with sub-arcsecond localization in our sample (GRB 160703A and GRB 160821A) using the 3.6m Devasthal Optical Telescope (DOT, Gupta et al. 2023). We conducted observations of GRB 160703A using TANSPEC (in i-filter, Sharma et al. 2022) on 2022-11-11, with a total exposure time of 5700 seconds. Similarly, observations of GRB 160821A were carried out using a 4K \times 4K IMAGER (in R-filter, Pandey et al. 2018, 2023) on 2022-12-20, with a total exposure time of 5100 seconds (see Figure A1 of the appendix). The methods for the optical data reduction of host images taken using TANSPEC and IMAGER are presented in Gupta et al. (2022b); Gupta (2023). However, despite our efforts, we were unable to detect any

associated host galaxies of these bursts within the best available error circles. Our observations yielded limiting magnitudes of ~ 23 mag for GRB 160703A and 23.6 mag for GRB 160821A, respectively. This suggests that the host galaxies of these GRBs may be intrinsically faint or highly obscured, reflecting the diverse nature of GRB host environments.

4. RESULTS

Utilizing the comprehensive analysis outlined above, we proceed to present the detailed spectro-polarimetric results of all five bright GRBs in the subsequent section.

4.1. Prompt uniform light curves and time-integrated spectra

The prompt light curve profiles of *Fermi* detected (GRB 160325A, GRB 160623A, GRB 160802A, and GRB 160821A) and *Swift* detected (GRB 160703A) GRBs in our sample are presented in Figure A2 of the appendix. The light curves of GRB 160325A (depicted in red) and GRB 160802A (in green) exhibit similar temporal profiles, characterized by two distinct episodes: a prominent pulse followed by a softer pulse, with a quiescent temporal gap in between. In contrast, GRB 160623A (highlighted in blue) showcases a primary pulse succeeded by weaker emission. Notably, *Fermi* could not detect the main emission of GRB 160623A due to Earth occultation during the burst's main emission, with the *Fermi* trigger occurring approximately 50 seconds post-burst (Mailyan et al. 2016). The light curve of GRB 160821A (depicted in pink) illustrates a faint initial emission followed by a very brighter emission. Meanwhile, GRB 160703A presents multiple overlapping profiles (in grey).

We employed the Bayesian block method on the CZTI Compton light curves to determine the time intervals for the time-integrated spectral analysis of GRBs in our sample. These selected time segments were also utilized for time-integrated polarization measurements, as detailed in section 2.2 of Chattopadhyay et al. 2022. The time-integrated *Fermi* spectra of GRB 160325A and GRB 160623A were optimally fitted using the `Bkn2pow` function. Conversely, the time-integrated *Fermi* spectra of GRB 160802A and GRB 160821A exhibited the best fits with the `Band + Blackbody` function. For the *Swift* BAT-detected GRB 160703A, the time-integrated spectrum was most effectively described by the `Cutoff power-law` function, considering the limitation of energy coverage of BAT. Detailed information regarding the best fit time-integrated spectral parameters for all five GRBs in our sample can be found in Table B1 of the appendix.

4.2. Comparison with Fermi GRBs

We analyzed the spectral (obtained using time-integrated analysis) and temporal parameters of GRBs in our sample and compared them with a larger sample of *Fermi* GBM detected GRBs (see Figure 1). Such comparison provides valuable insights into the spectral properties and diversity of these cosmic sources. The distribution of the low energy photon index is useful for characterizing the power-law behavior of the photon spectrum at lower energies and identifying the emission mechanisms. The distribution of α_{pt} reveals that a significant number of bursts deviates from the synchrotron emission mechanism. The distribution of E_{p} value is crucial and indicates the energy at which the GRB spectrum reaches its maximum intensity. We noted all the bursts in our sample have a harder peak energy than the mean peak value obtained for *Fermi* GBM detected GRBs. The distribution of high-energy photon indices signifies the steepness of the spectral slope in the high-energy regime. The high energy spectral index (β_{pt}) values (calculated using the time-integrated spectral measurement) for GRB 160325A, GRB 160623A, and GRB 160802A are steeper than the mean value obtained for *Fermi* GBM detected GRBs. On the other hand, GRB 160821A has a shallower β_{pt} value. Further, we studied the distribution of T_{90} duration using *Fermi* GBM data, and the distribution indicates that all the bursts in our sample belong to the long GRBs class.

4.2.1. Energy-fluence distribution

We compared the energy fluence value of GRBs in our sample with *Fermi* GBM and *Swift* BAT detected GRBs. Our analysis indicates that GRBs in our sample are significantly brighter than the mean value of observed fluence values (see Figure 1). We also represented this result using the distribution of T_{90} as a function of energy fluence values for the bursts observed by *Fermi* GBM (see inset plot in Figure 1). High fluence bursts are useful for polarization measurements.

4.2.2. Spectral-Hardness plot

The classification of GRBs primarily relies on the prompt emission properties, such as the duration of the T_{90} and the hardness ratio. We studied the spectral hardness distribution for the GRBs in our sample. The peak energy of a GRB's spectrum is related to its duration. Studies have shown that GRBs with longer durations tend to have lower peak energies (soft), while shorter-duration GRBs tend to have higher peak energies (hard). We compiled the T_{90} duration and E_{p} values of all the GRBs detected by the *Fermi* GBM instrument from the GBM burst catalog. We noted that all

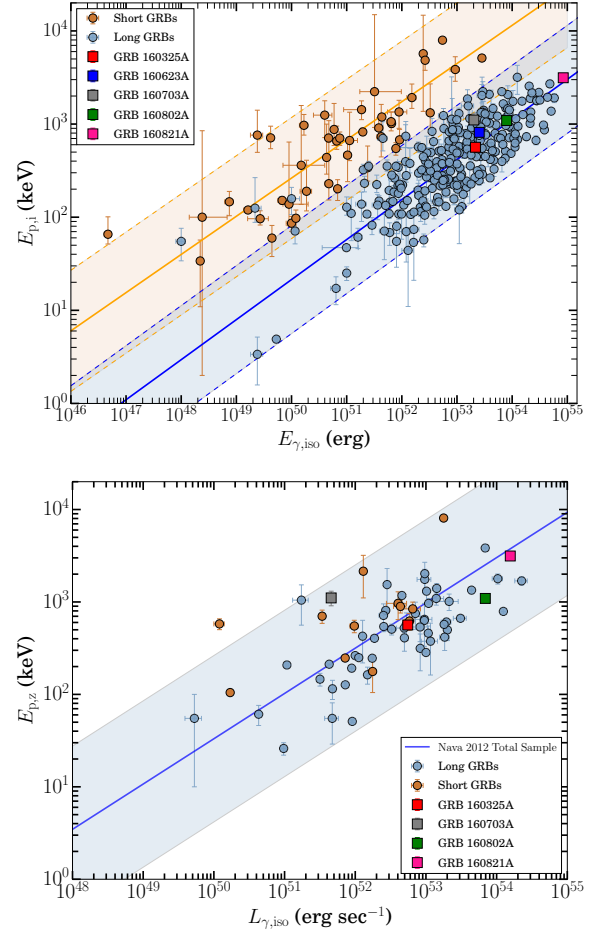


Figure 2. Prompt emission correlation of GRBs: Top: The location of five bright GRBs in Amati correlation. The well-studied long and short bursts extracted from Minaev & Pozanenko (2020) are represented by blue and orange circles, respectively, with solid blue and orange lines depicting the linear fits for these groups. The parallel shaded areas illustrate the 3σ variation. Bottom: The location of five GRBs in Yonetoku correlation. The well-studied long and short bursts, as studied in Nava et al. (2012), are shown with blue and orange circles. The parallel shaded areas indicate the 3σ scatter. The colored squares illustrate the location of the GRBs of our sample. In our analysis, we included all five GRBs in the Amati and Yonetoku relations. However, for the GRBs without measured redshifts, we assumed a redshift value of 2, mean of redshift distribution for long GRBs (Gupta et al. 2022b).

the GRBs in our sample are consistent with the typical characteristics of long GRBs (see Figure 1).

4.2.3. Amati and Yonetoku correlation

Several global correlations can be observed in the prompt properties of GRBs, and these correlations play a crucial role in characterizing GRBs (Minaev & Pozanenko 2020). We studied the Amati correlation for the

GRBs in our sample (Amati 2006). It is a well-known empirical relationship and relates the isotropic equivalent energy ($E_{\gamma,\text{iso}}$) and the spectral peak energy of GRB prompt emission spectra in the rest frame. Amati correlation has important implications for the physics of the prompt emission process, the emission mechanism, or the properties of the GRB progenitor systems. For GRB 160623A, we obtained $E_{\gamma,\text{iso}}$ and peak energy values using *Konus-Wind* observations (Tsvetkova et al. 2017) as the main emission was not detected using *Fermi* GBM. We noted that all the GRBs in our sample are consistent with the Amati correlation of the long GRBs (see Figure 2). The physical explanation for the Amati correlation in the literature remains a subject of debate and lacks consensus. Nevertheless, certain studies suggest that the Amati correlation may be attributed to the viewing angle effect within the context of synchrotron emission (Yamazaki et al. 2004; Eichler & Levinson 2004; Levinson & Eichler 2005).

We also studied the Yonetoku correlation for our sample (Yonetoku et al. 2010). The Yonetoku correlation relates two observables of GRBs: $E_{\gamma,\text{iso}}$ and the peak luminosity ($L_{\gamma,\text{iso}}$) of the prompt gamma-ray emission. This correlation indicates that GRBs with higher isotropic equivalent energies tend to have higher peak luminosities. The correlation provides constraints and insights into the nature of GRB progenitors, emission processes, and the energy release mechanisms associated with these powerful cosmic explosions. This correlation could potentially be explained by the photospheric dissipation model, taking into account that subphotospheric dissipation occurs at a considerable distance from the central engine (Rees & Mészáros 2005). We noted that all the GRBs in our sample are consistent with the Yonetoku correlation (see Figure 2). Furthermore, the photospheric model has been useful in explaining both the Amati and Yonetoku relations. Recent studies have shown that these correlations can be naturally accounted for by considering the effects of the viewing angle relative to the jet axis. When the photospheric emission is viewed at different angles, the observed spectral properties and the inferred energetics can vary significantly. This variation can lead to the observed Amati and Yonetoku relations (Ito et al. 2019; Parsotan & Ito 2022; Ito et al. 2024; Parsotan & Lazzati 2022).

4.3. Time-resolved spectral measurements

The GRBs spectrum shows strong evolution within the burst; therefore, the derived time-integrated spectral parameters may not provide intrinsic spectral behavior and can be artifacts due to strong spectral evo-

lution. Thus, time-resolved spectral measurements are needed to verify the underlying radiation mechanisms of GRBs. We studied the time-resolved spectral analysis of those bursts (GRB 160325A, GRB 160802A, and GRB 160821A) for which *Fermi* GBM observations were available. *Fermi* GBM wide spectral coverage is crucial for detailed spectral analysis.

We selected the temporal bins for time-resolved spectral analysis using the Bayesian Block method. After selecting bins, we calculated the significance of individual bins and only selected those with a significance greater than 10. Further, we fitted all these bins with **Band** and **CPL** models and calculated the difference of DIC values to identify the best-fit model for individual bins. The comparison between DIC values of **Band** and **CPL** models for all three GRBs are plotted with red squares in Figure A3 of the appendix. The DIC comparison indicates that individual bins of GRB 160325A, GRB 160802A, and GRB 160821A are preferred **Band** function over **CPL** model (no bins have $\Delta \text{DIC} \leq -10$). For some of the bins, **CPL** model has ΔDIC value in between zero and -10, indicating that **Band** and **CPL** both models have an equivalent fit. After selecting the best-fit function between **Band** and **CPL** models, we added the additional **Blackbody** (BB) function. We again selected the best-fit model between **Band** or **CPL** with **Band+BB** or **CPL+BB** using the difference of DIC values obtained for the two models. A detailed selection method for the different empirical functions is present in Caballero-García et al. (2023). Furthermore, we have also compared the fits between the best fit empirical and physical models. However, there are some time bins for which the physical synchrotron parameters are not very well constrained (due to the low significance).

We used the derived spectral parameters using time-resolved spectral analysis to study their evolution and correlation among them. The spectral evolution of empirical parameters E_p , low and high energy photon indices for GRB 160325A, GRB 160802A, and GRB 160821A is presented in Figures 3, 4, and 5, respectively. The evolution of physical parameters (electron spectral index and magnetic field strength) obtained using synchrotron modeling is also shown in these figures. We observed that E_p evolution of all three GRBs has an intensity tracking behavior. Additionally, α_{pt} evolution for GRB 160802A and GRB 160821A have the same tracking behavior, supporting a double-tracking nature. The correlation among different empirical and physical spectral parameters of time-resolved spectral parameters was also studied. The correlation results between different model parameters are listed in the appendix in Table B11. Our correlation analysis indicates that

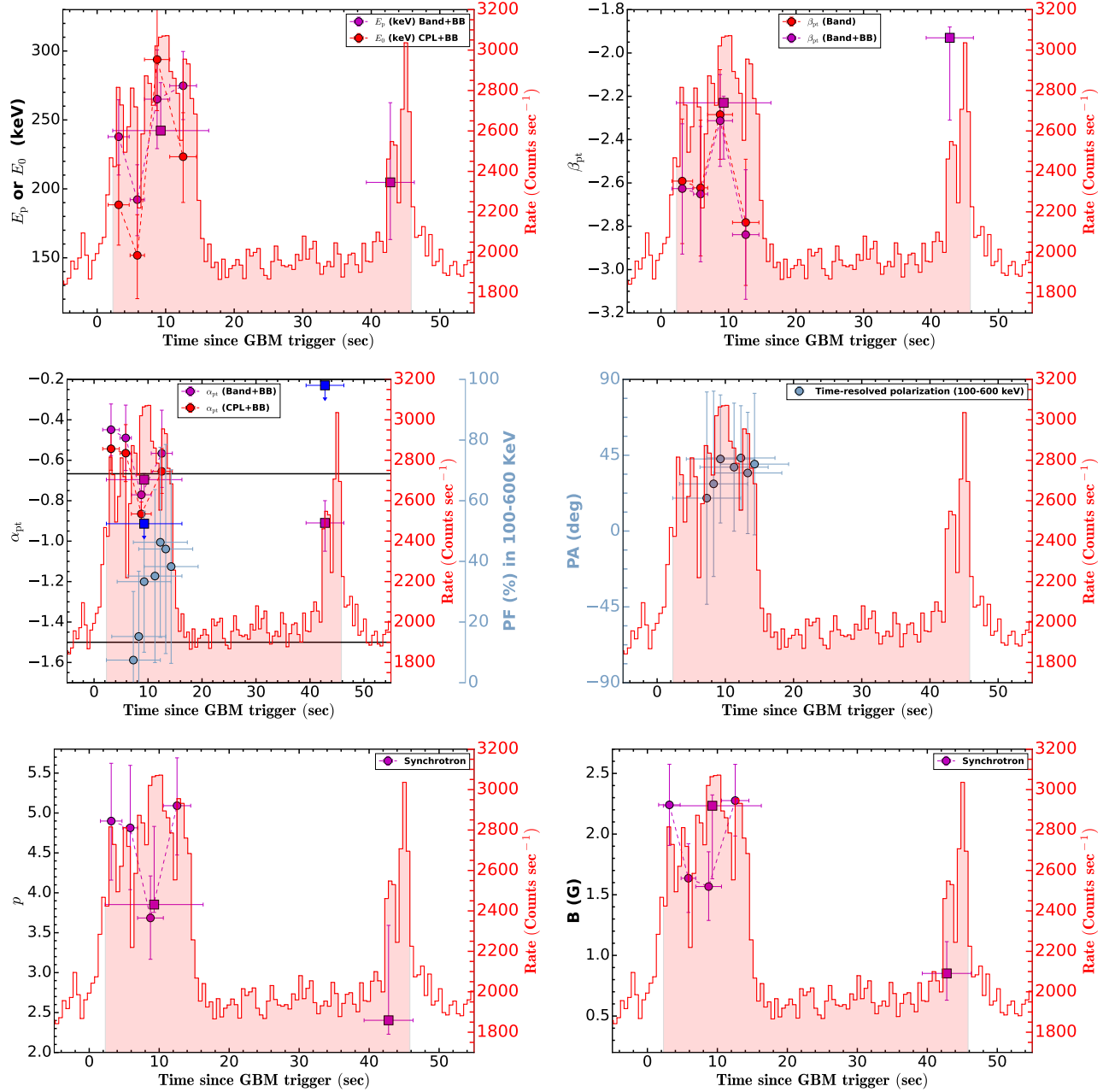


Figure 3. Time-resolved spectro-polarimetric characteristic of GRB 160325A. Top-left: Temporal evolution of peak energy or cutoff energy obtained using empirical spectral fitting. Top-right: Temporal evolution of high energy photon index. Middle-left: Temporal evolution of low energy photon index. The black solid lines correspond to the theoretically predicted values of the low energy photon index from thin-shell synchrotron emission models. The pulsed-wise time-resolved polarization fraction is shown using blue squares. The right side y-scale (light blue) represents the evolution of polarization fraction over time obtained using time-resolved polarization analysis (sliding mode). Middle-right: Temporal evolution of polarization angle over time obtained using time-resolved polarization analysis (sliding mode). Bottom-left: Temporal evolution of the power-law index of the energy distribution of injected electron obtained using physical spectral fitting. Bottom-right: Temporal evolution of the strength of the magnetic field. Squares show the results for pulse-wise time-resolved spectro-polarimetric analysis.

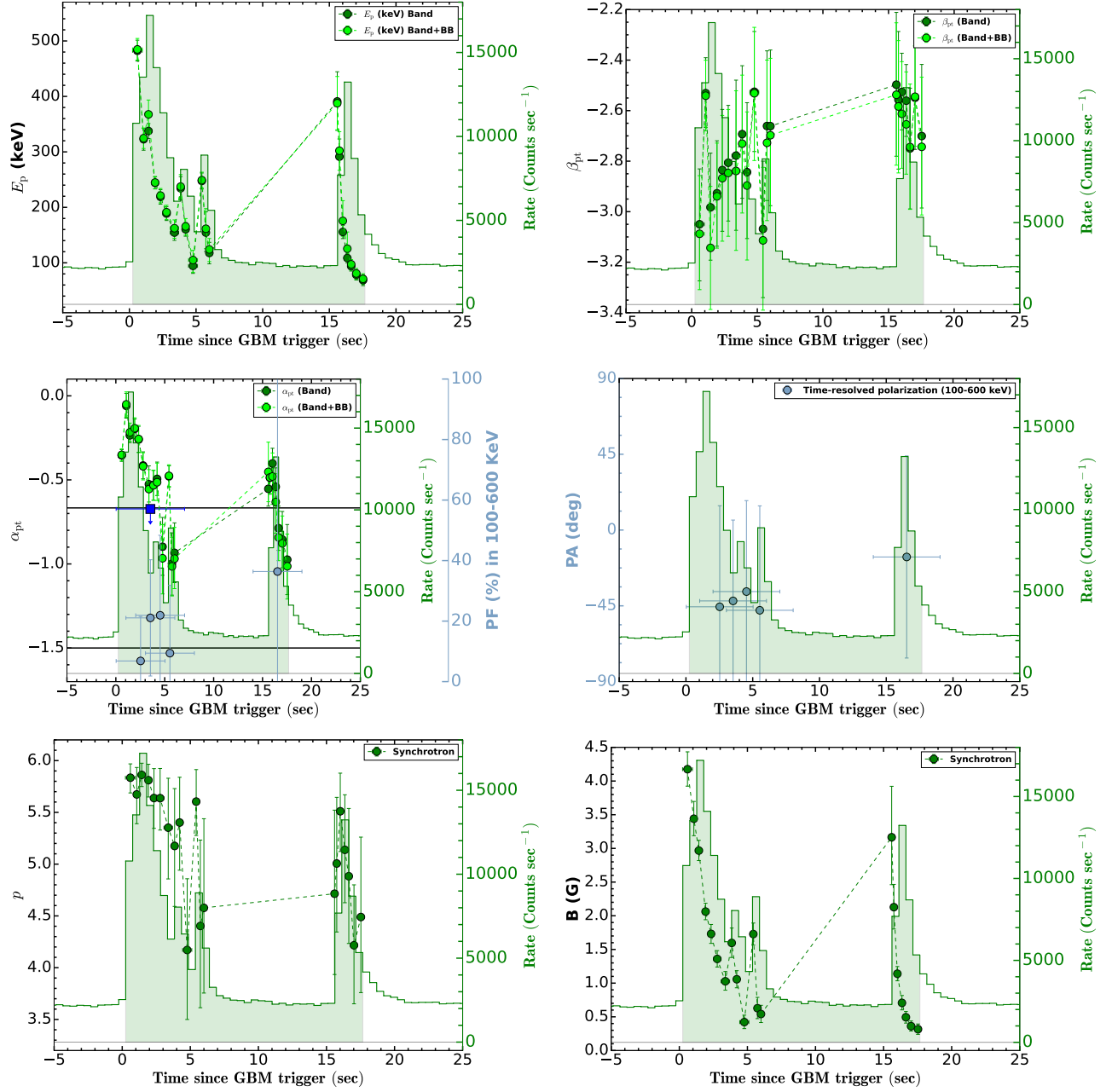


Figure 4. Time-resolved spectro-polarimetric characteristic of GRB 160802A. Top-left: Temporal evolution of peak energy obtained using empirical spectral fitting of GRB 160802A. Top-right: Temporal evolution of high energy photon index. Middle-left: Temporal evolution of low energy photon index. The pulsed-wise time-resolved polarization fraction is shown using blue squares. The right side y-scale (light blue) represents the evolution of polarization fraction over time obtained using time-resolved polarization analysis (sliding mode). Middle-right: Temporal evolution of polarization angle over time obtained using time-resolved polarization analysis (sliding mode). Bottom-left: Temporal evolution of the power-law index of the energy distribution of injected electron obtained using physical spectral fitting. Bottom-right: Temporal evolution of the strength of the magnetic field.

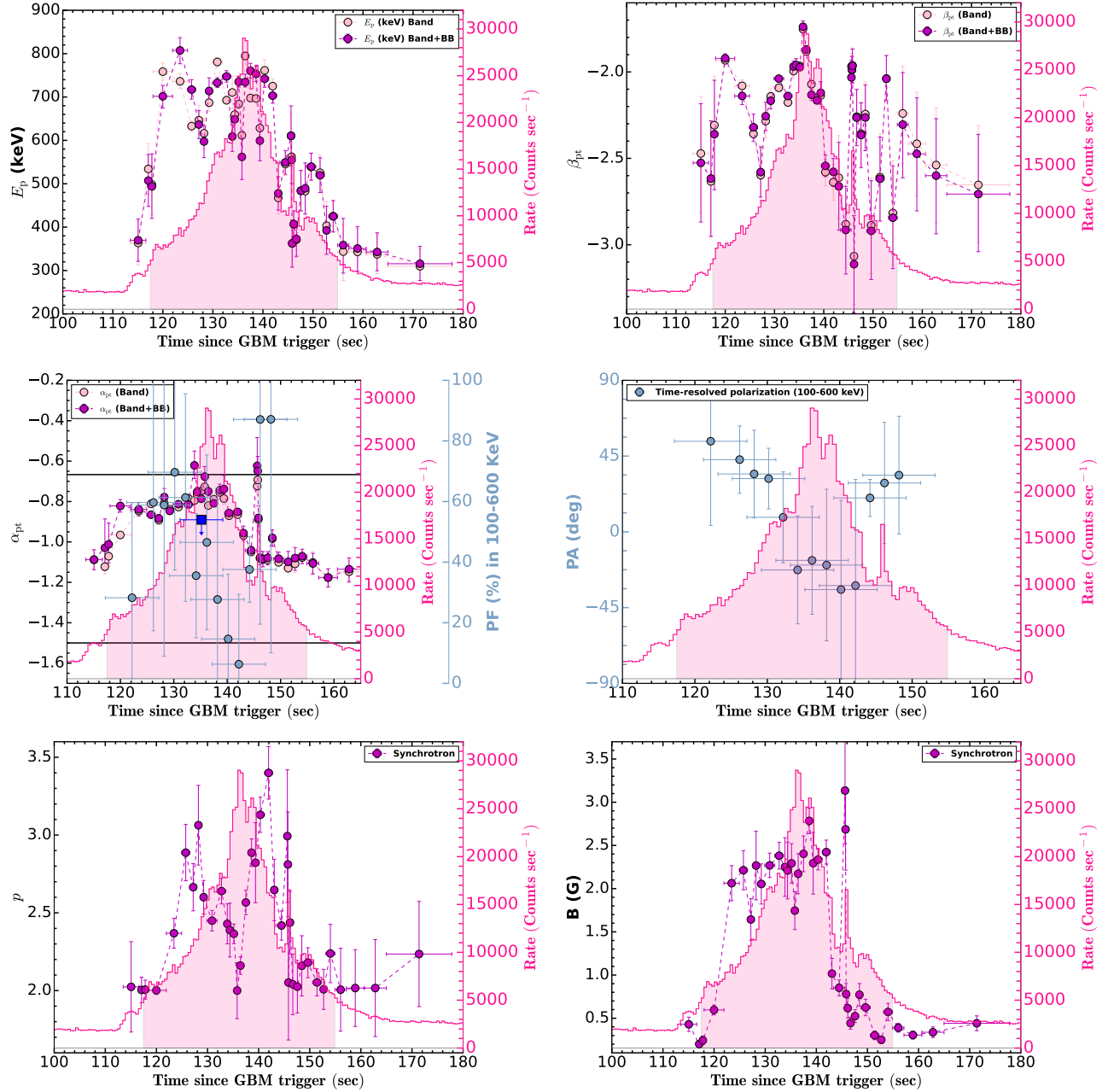


Figure 5. Time-resolved spectro-polarimetric characteristic of GRB 160821A. Top-left: Temporal evolution of peak energy obtained using empirical spectral fitting of GRB 160821A. Top-right: Temporal evolution of high energy photon index. Middle-left: Temporal evolution of low energy photon index. The pulsed-wise time-resolved polarization fraction is shown using blue squares. The right side y-scale (light blue) represents the evolution of polarization fraction over time obtained using time-resolved polarization analysis (sliding mode). Middle-right: Temporal evolution of polarization angle over time obtained using time-resolved polarization analysis (sliding mode). Bottom-left: Temporal evolution of the power-law index of the energy distribution of injected electron obtained using physical spectral fitting. Bottom-right: Temporal evolution of the strength of the magnetic field.

the peak energy of the burst (obtained using empirical fitting) is strongly correlated with flux evolution for all three GRBs. We also observed that α_{pt} is strongly correlated with flux evolution for GRB 160802A and GRB 160821A. However, it is anti-correlated for GRB

1603025A (correlation analysis for GRB 160325A is not statistically significant due to less number of available bins). The physical parameters B and p calculated using synchrotron modeling are found to be correlated with each other for GRB 160802A and GRB 160821A. More-

over, the physical parameters B and p strongly correlate with empirical parameters E_p , α_{pt} , and flux for GRB 160802A and GRB 160821A.

4.4. Time-resolved polarization measurements

Previous studies on the polarization of a few GRBs, such as GRB 100826A, GRB 160821A, and GRB 170114A, have suggested that their polarization properties could exhibit temporal evolution (Yonetoku et al. 2011a; Sharma et al. 2019; Burgess et al. 2019). However, it's important to note that these GRBs were observed using different instruments and analyzed through distinct pipelines. The observed hints regarding the evolution in polarization properties of GRB 100826A, GRB 160821A, and GRB 170114A were obtained using the GAP, *AstroSat*/CZTI, and POLAR instruments, respectively. These findings imply that the polarization properties of GRBs may undergo intrinsic changes over time, potentially resulting in null or low polarization fractions in time-integrated polarization measurements.

In our recent five-year catalog paper (Chattopadhyay et al. 2022), we highlighted a notable observation: approximately 75% of GRBs exhibit low or null polarization fractions in our time-integrated polarization analysis. However, to ascertain whether these bursts are intrinsically unpolarized or if their polarization properties undergo changes within the bursts, leading to null or low polarization, a detailed time-resolved polarization analysis is imperative. In the present work, we studied a detailed time-resolved polarization analysis of five GRBs detected in the first year of operation of *AstroSat*. We applied two distinct binning techniques to the GRB light curves and subsequently conducted polarization measurements. In case the GRB light curve has more than one pulse (for example, GRB 160325A and GRB 160802A), we selected individual pulses for time-resolved polarization measurement. Conversely, for GRBs exhibiting a single pulse, namely GRB 160623A, GRB 160703A, and GRB 160821A, we selected the peak duration of the burst. The results of our time-resolved polarization measurement are tabulated in Table 2. Additionally, we present an illustrative example of the posterior probability distribution obtained through polarization analysis of GRB 160623A (during the peak duration) in Figure 6.

Further, we also selected the time bins using the sliding mode temporal binning method (since the GRB light curves exhibit rapid or irregular variations) with a bin width of 10 sec (for GRB 160325A, GRB 160623A, GRB 160703A, and GRB 160821A) or 5 sec (for GRB 160802A) for the time-resolved polarization measurements. We initially divided the light curve into smaller

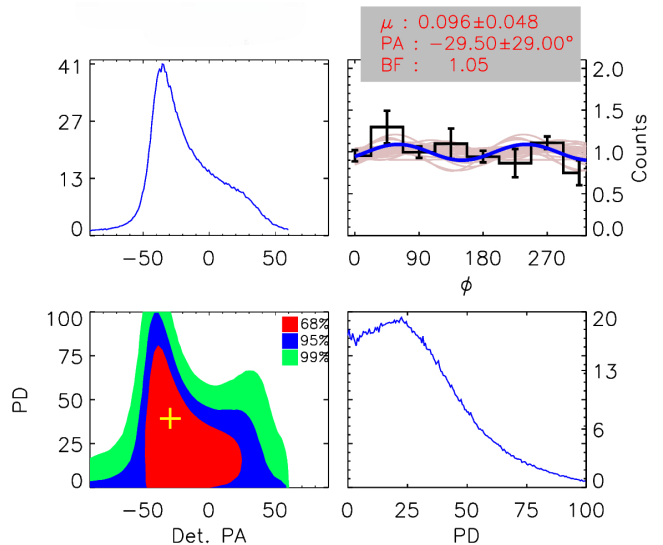


Figure 6. An example of the posterior probability distribution (polarization angle in the top left and polarization degree in the bottom right) obtained using polarization analysis (using MCMC) of GRB 160623A (during the peak duration). In the top right panel, the modulation curve and the sinusoidal fit are illustrated by a solid blue line, accompanied by 100 random Markov Chain Monte Carlo (MCMC) iterations. In the bottom left panel, the confidence area for the polarization angle and degree is represented by red, blue, and green contours, corresponding to confidence levels of 68%, 95%, and 99%, respectively.

time intervals of the bin width from 0-10 sec or 0-5 sec and slid these average intervals across the entire duration of the burst with increasing order of 1 sec (GRB 160325A, GRB 160623A, GRB 160703A, and GRB 160802A) or 2 sec (GRB 160821A). Using the sliding mode binning, we calculated the average values of polarization parameters within each bin. The polarization results obtained using the temporal sliding binning along with pulsed/peak-wise binning algorithms are displayed in Figures 3, 4, 5, and 7, respectively. The time-resolved (pulsed-wise) analysis of the first pulses of GRB 160325A and GRB 160802A constrains the higher PF values (see Table 2), although sliding mode analysis of the same pulses indicates lower PF values. We noted that the polarization angles of GRB 160325A, GRB 160623A, GRB 160703A, and GRB 160802A obtained for different burst intervals remain within their respective error bars. This suggests that there is no substantial change in the polarization properties as these bursts evolve. However, we noted that the polarization angles of GRB 160821A changed twice within the burst, consistent with our previous results reported in 100-300 keV with the previous polarization pipeline (Sharma et al. 2019). Our time-resolved polarization analysis gives a

Table 2. The calculated values of time-resolved polarization fraction (pulsed or peak-wise time bins) of all the five bursts in 100-600 keV.

GRB name	Time interval (sec)	No. of Compton events	PF (%)	BF
GRB 160325A	2.28-16.28	556	< 52.42	0.75
GRB 160325A	39.28-46.28	144	< 98.04	2.78
GRB 160623A	5.16-10.16	1089	< 58.86	1.05
GRB 160703A	0.22-9.22	172	unconstrained	0.80
GRB 160802A	0.03-7.03	1234	< 57.06	0.90
GRB 160802A	14.03-19.03	273	unconstrained	0.79
GRB 160821A	131.18-139.18	1246	< 53.98	1.87

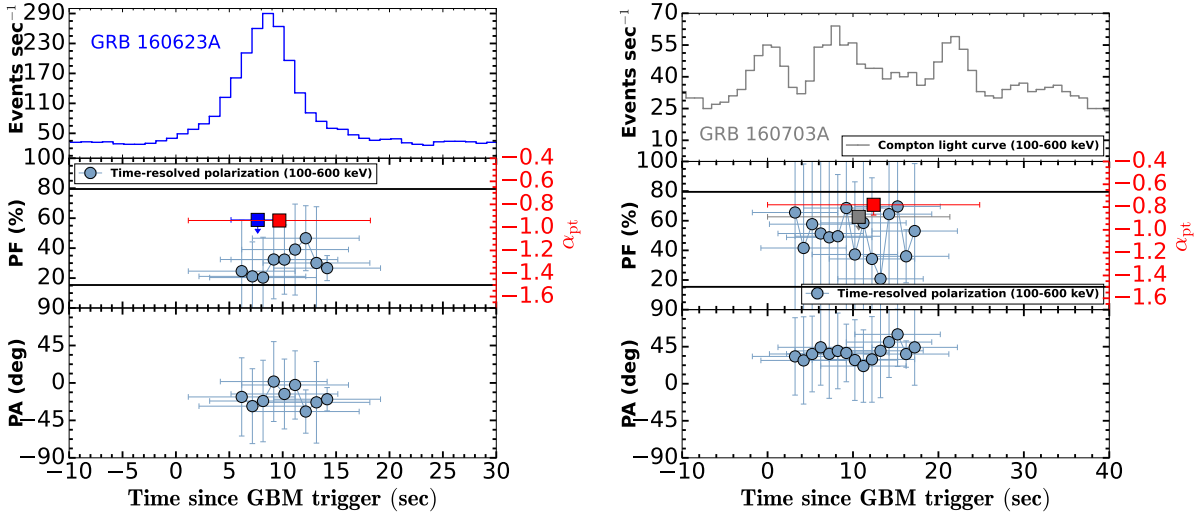


Figure 7. Time-resolved polarization analysis of GRB 160623A (left) and GRB 160703A (right). Top panels: 1-sec bin size Compton light curves obtained using CZTI data. Middle panels: The evolution of PF over time (time-sliding mode). The PF obtained during the peak or averaged analysis is shown using blue (GRB 160623A) and grey (GRB 160703A) squares, respectively. The right side Y-scales (red) show the values of α of GRB 160623A and GRB 160703A, respectively. The black solid lines correspond to the theoretically predicted values of the low energy photon index from thin-shell synchrotron emission models. Bottom panels: The evolution of PA over time (time-sliding mode).

hint that the polarization properties of GRB 160821A depend on the temporal window of the burst.

4.5. Energy-resolved polarization measurements

In addition to conducting time-resolved polarization measurements, we also performed an energy-resolved polarization analysis. A comparison of the polarization fraction obtained using the *AstroSat* CZTI and POLAR missions catalog revealed that *AstroSat* CZTI detected approximately 20 % higher polarization compared to POLAR measurements (Chattopadhyay et al. 2022). We suggested that the discrepancy between the observed time-integrated and energy-integrated polarization fractions of prompt emission by *AstroSat* CZTI and POLAR missions could be attributed to the fact that both instruments report the polarization fractions values in different energy channels (CZTI values in 100-600 keV, and POLAR values in 50-500 keV).

In this work, we carried out energy-resolved polarization measurements to investigate the energy-dependent behavior of polarized radiation (polarization degree and angle) during the prompt phase of GRBs. We have employed two methods for selecting energy bins of individual bursts. Initially, we selected the bins based on observed peak energy calculated from the time-averaged spectral analysis. We created two bins: one ranging from $100-E_p$ keV and the other from E_p-600 keV. In cases where the observed peak energy exceeded 600 keV (the maximum allowed energy range for the polarization measurements using CZTI), we selected the following bins: 100-300 keV and 300-600 keV, considering that the mean value of peak energy for long GRBs is approximately 200-300 keV (refer to Figure 1). The calculated values of the energy-resolved polarization fraction of all five bursts are listed in Table 3.

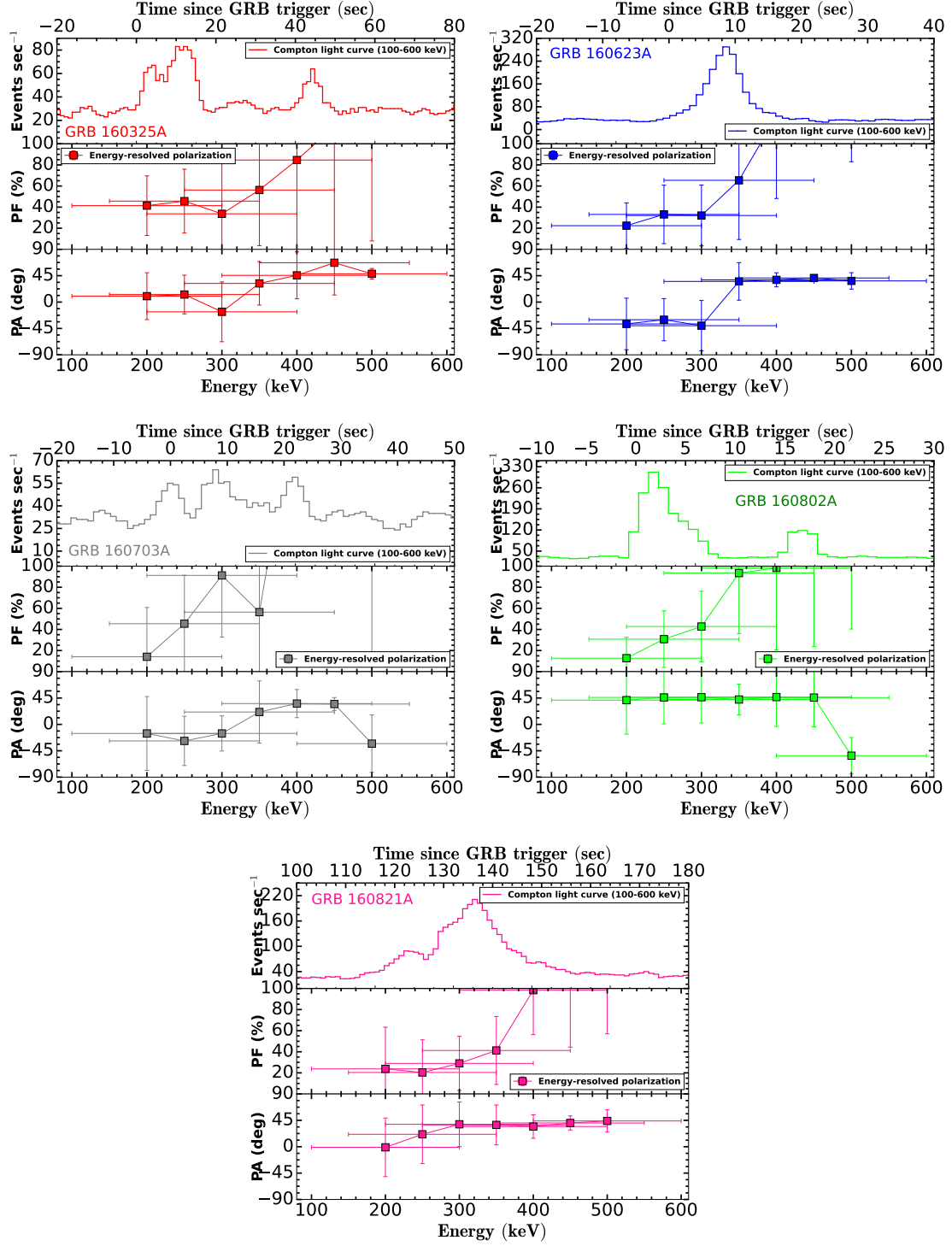


Figure 8. Energy-resolved polarization measurements: Top: Compton light curves of the GRBs with 1-sec bin size obtained using CZTI data. Middle and bottom: The evolution of polarization fraction and polarization angle with energy. The energy binning has been carried out based on the sliding mode algorithm.

Further, we also selected the energy bins using the sliding mode spectral binning method (since the GRB spectra exhibit rapid variations) with a bin width of 50 keV for the energy-resolved polarization of all five GRBs in our sample. We initially divided the spectrum into smaller energy intervals of the bin width from 100-300 keV and slid these average energy intervals across the total energy range of the CZTI with an increasing order of 50 keV. Using the sliding mode binning, we calculated the average values of polarization parameters within each spectral bin. The polarization results obtained using the energy sliding binning algorithm are shown in Figure 8. We noted that the polarization angles of GRB 160325A, GRB 160703A, and GRB 160802A, GRB 160821A obtained for different energy segments remain mostly consistent (no substantial change in the polarization angles); however, we noted that the polarization angles of GRB 160623A changed with energy. Additionally, we noted that the polarization fraction values have increasing trends with energy, although the analysis might be limited due to fewer Compton counts in later energy bins. The energy-resolved polarization analysis gives a hint that polarization measurements depend on the energy channels of the detectors.

5. DISCUSSION

Based on the above data analysis and results, we present the key discussion on the spectro-polarimetric properties of individual GRBs in this section.

5.1. Jet composition and emission mechanisms of the sample

The main objective of this study is to investigate the possible jet composition and emission mechanisms of GRBs through time-resolved and energy-resolved spectro-polarimetric analysis. Different radiation models in GRBs are associated with different polarization fraction values. However, it is important to note that the observed polarization fraction values also depend on the viewing geometry of the bursts. To assess the viewing geometry of individual bursts, we employed the $\Gamma\theta_j$ condition. By applying this condition, we sought to gain insights into the viewing perspective of the bursts and their implications on their polarization properties. When viewing the jet from an on-axis perspective, the value of $\Gamma\theta_j$ is significantly greater than 1. Conversely, for off-axis observations, $\Gamma\theta_j$ is expected to be much smaller than 1. In the case of a narrow jetted view, the $\Gamma\theta_j$ value is expected to be approximately 1. The value of Γ of the fireball can be derived from prompt emission as well as afterglow features of GRBs (Liang et al. 2010; Ghirlanda et al. 2018). In this work, we constrain the

value of bulk Lorentz factor using well-studied Liang correlation³, the strong correlation between bulk Lorentz factor and isotropic gamma-ray energy of the fireball (Liang et al. 2010). The derived values of bulk Lorentz factor are tabulated in Table 4. For GRB 160623A, we obtained $E_{\gamma,\text{iso}}$ value using *Konus-Wind* observations (Tsvetkova et al. 2017) as the main emission was not detected using *Fermi* GBM. Additionally, we derive the jet opening angle (lower limits) using the X-ray afterglow light curves observed using *Swift* XRT and equation 4 of Frail et al. (2001). The θ_j value depends on micro-physical afterglow parameters (medium number density (n_0) and electrons thermal energy fraction (ϵ_e)). We assume typical values of $n_0 = 1$ and $\epsilon_e = 0.2$ to constrain θ_j values (Gupta et al. 2022c). However, detailed afterglow modeling and a good data set will be needed to constrain these parameters better (Gupta et al. 2022a). For GRB 160623A, we obtained the θ_j value from Chen et al. (2020). However, in the case of GRB 160802A and GRB 160821A, no *Swift* XRT observations are available, so we used $\theta_j = 2.1$ degree, which is the mean value of jet opening angle for typical *Fermi*-detected long GRBs (Sharma et al. 2021). After calculating the bulk Lorentz factor and jet opening angle values for individual bursts, we determine the viewing geometry ($\Gamma\theta_j$). The calculated values of $\Gamma\theta_j$ are tabulated in Table 4. We noted that the calculated for all five bursts in our sample have $\Gamma\theta_j \gg 1$, suggesting that the jet from these GRBs is observed from an on-axis perspective. Further, we utilized $\Gamma\theta_j$ condition and our spectro-polarimetric results for each of the five GRBs in our sample to investigate GRBs' possible jet composition and emission mechanisms.

5.1.1. GRB 160325A

We studied the spectro-polarimetric properties (analysis of spectral properties using *Fermi* as well as the polarization of emitted radiation using *AstroSat*) of GRB 160325A for both pulses (the light curve of this burst exhibits two separate emission episodes with a quiescent period in between). The α_{pt} values seem harder during the first episode, and we observed a low polarization fraction (using time-resolved polarization measurements) during this episode. Conversely, α_{pt} value becomes softer during the second emission episode, and we observed a hint of high polarization fraction (an upper limit of 98 %). The observed spectro-polarimetric properties during the first episode suggest that the emission during this episode originated from a thick shell photosphere with localized dissipation occurring below

³ $\Gamma_0 \approx 182 \times E_{\gamma,\text{iso},52}^{0.25 \pm 0.03}$

Table 3. The calculated values of energy-resolved polarization fraction (100- E_p or 300 keV and E_p or 300 -600 keV) of all the five bursts in our sample.

GRB name	Energy range (keV)	No. of Compton events	PF (%)	BF
GRB 160325A	100-187	391	< 70.54	1.41
GRB 160325A	187-600	380	< 33.28	0.80
GRB 160623A	100-300	1428	< 24.42	0.74
GRB 160623A	300-600	277	unconstrained	2.82
GRB 160703A	100-351	376	< 18.64	0.73
GRB 160703A	351-600	51	unconstrained	1.02
GRB 160802A	100-363	1360	< 27.92	0.70
GRB 160802A	363-600	152	< 69.97	0.69
GRB 160821A	100-300	2387	< 20.03	0.85
GRB 160821A	300-600	468	unconstrained	2.27

Table 4. The calculated values of the Lorentz factor and jet opening angle of all the five bursts in our sample. $\Gamma\theta_j \gg 1$ suggests that the jet from all the GRBs in our sample is observed from an on-axis view.

GRB name	$E_{\gamma,iso} \times 10^{52}$ (erg)	Γ	θ_j (degree)	$\Gamma\theta_j$
GRB 160325A	21.63	392.48	> 1.32	~ 9.05
GRB 160623A	25.3	408.17	> 13	~ 92.61
GRB 160703A	20.27	386.18	> 4.68	~ 31.52
GRB 160802A	79.44	543.36	> 2.1	~ 19.91
GRB 160821A	844.03	980.98	> 2.1	~ 35.95

it. In contrast, the emission during the second episode is dominated by thin-shell synchrotron emission. Furthermore, our time-resolved polarization measurements of GRB 160325A indicate the transition of a baryonic-dominated jet composition during the first episode to a subdominant Poynting flux jet composition during the second episode. Our results (with an updated polarization analysis pipeline) are consistent with our previous spectro-polarimetric analysis of the bursts reported in 100-300 keV (Sharma et al. 2020).

5.1.2. GRB 160623A

The prompt light curve of GRB 160623A obtained using *Konus-Wind* exhibits a broad emission episode (main), followed by a weaker emission episode (Frederiks et al. 2016a). However, the main emission episode of GRB 160623A was occluded for *Fermi* mission. Therefore, we utilized the time-integrated spectral analysis results reported by us using *Konus-Wind* observations to constrain the radiation mechanism of GRB 160623A (Chattopadhyay et al. 2022). We noted that the observed value of α_{pt} using the time-integrated *Konus-Wind* spectrum lies within the synchrotron slow and fast cooling prediction. Additionally, the time-integrated and time-resolved (however, it is important to note that within a 2-sigma confidence interval, these polarization measurements are consistent with low polarization) po-

larization analysis using CZTI data gives a hint for the high degree of polarization, supporting the synchrotron emission in an ordered magnetic field (see Figure 7). The possibility of no significant polarization cannot be entirely ruled out based on the current measurements. Our spectro-polarimetric analysis of GRB 160623A suggests a Poynting flux jet composition throughout the burst's emission.

5.1.3. GRB 160703A

The light curve of GRB 160703A, as observed by *Konus-Wind*, displays multiple overlapping emission pulses (Frederiks et al. 2016b), consistent with *Swift* BAT light curve (see Figure A2 of the appendix). However, since this GRB was not detected by the *Fermi* mission, we were unable to perform a detailed time-resolved spectral analysis of this burst. To investigate the radiation mechanism of GRB 160703A, we relied on the time-integrated spectral analysis results previously reported by us using *Konus-Wind* observations (Chattopadhyay et al. 2022). The low energy photon index obtained from the time-integrated *Konus-Wind* spectrum is consistent with the synchrotron emission model. Furthermore, our α_{pt} value calculated using the time-integrated *Swift* BAT spectral analysis is also consistent with the synchrotron emission model (see Table B1 of the appendix). Similar to the previous case, both the

time-integrated and time-resolved (however, it is important to note that the observed polarization is also consistent with low polarization within 2-sigma confidence interval) polarization analysis using *AstroSat* CZTI data provide indications of a hint for the high degree of polarization, supporting the presence of synchrotron emission in an ordered magnetic field (see Figure 7). Our spectro-polarimetric analysis of GRB 160703A suggests a Poynting flux jet composition throughout the emission of the burst.

5.1.4. GRB 160802A

The light curve of GRB 160802A displays two distinct emission episodes separated by a quiescent period (see Figure A2 of the appendix). A detailed spectro-polarimetric analysis was conducted for both episodes, revealing a notable similarity in spectral behavior to GRB 160325A. The spectral analysis of GRB 160802A indicates that the low energy photon index remains (hard) above the synchrotron emission “line of death” for most of the temporal bins in the first episode (see Figure 4). Time-resolved polarization measurements (sliding mode analysis) during this episode constrain the polarization fraction to low values. Since the jet of this burst was observed on-axis (see section 5.1), our spectro-polarimetric analysis of the first episode is consistent with the photospheric emission model. Such hard values of α_{pt} and low polarization fraction can be explained using a Baryonic dominated jet with subphotospheric dissipation. In contrast, α_{pt} value becomes softer (than the first episode) during the second emission episode. Although we obtained a hint of a high degree of polarization fraction (with respect to the time-resolved measurements during the first episode), we were unable to obtain a more precise measurement due to the low number of Compton counts during this episode. The observed spectro-polarimetric properties during the second episode suggest that it is dominated by thin-shell synchrotron emission. Furthermore, our time-resolved polarization measurements of GRB 160802A suggest a possible transition of a baryonic-dominated jet composition during the first episode to a subdominant Poynting flux jet composition during the second episode. However, the limited number of Compton events during the second episode of GRB 160802A prevents us from making a definitive claim for such a transition.

5.1.5. GRB 160821A

The light curve of GRB 160821A observed by *Fermi* GBM reveals an initial fainter emission followed by a highly intense emission. However, the initial weaker emission was not detected by *AstroSat* CZTI. Therefore, this study focuses solely on the spectro-polarimetric

analysis of the main emission episode of GRB 160821A. The exceptional brightness of the main emission episode of GRB 160821A helps us to perform a detailed time-resolved spectro-polarimetric analysis of the burst. The observed evolution of α_{pt} lies within the predicted range of the thin shell synchrotron emission model. The high flux suggests that the bursts are observed on-axis, as discussed in Section 5.1. During the rising and peak phase of the main pulse, we observed the swing in the polarization angle by approximately 90 degrees. Subsequently, from the peak to the decay phase of the pulse, the polarization angle swings back. Our time-resolved polarization analysis indicates that the lower value of the time-integrated polarization fraction reported in Chattopadhyay et al. (2022) may be attributed to the variation in the polarization angle. The spectro-polarimetric analysis of GRB 160821A provides further support for synchrotron emission occurring within an ordered magnetic field. The results also suggest that the jet composition throughout the burst’s emission is dominated by Poynting flux. These results align with our previous spectro-polarimetric analysis of bursts reported in the 100-300 keV energy range (Sharma et al. 2019).

6. SUMMARY AND CONCLUSION

The spectro-polarimetric analysis of GRBs has been investigated for a limited number of GRBs, and most of the studies explored only the time-integrated polarization measurements due to the transient behavior of GRBs, in particular, as well as the challenge of X-ray polarization measurement, in general, (Gill et al. 2020; Kole et al. 2020; Chattopadhyay et al. 2022). In our recent study, we suggested that the majority of bursts in the sample exhibit minimal or no polarization in our time-integrated measurements within the 100-600 keV energy range, as observed with *AstroSat* CZTI (Chattopadhyay et al. 2022). However, a detailed time-resolved and energy-resolved polarization analysis was needed to identify if the observed low-polarization fraction is intrinsic or due to variation in polarization fraction and polarization angle with time and energy within the burst. In this paper, we investigated the prompt emission temporal, spectral, and polarization properties of five bright bursts observed using the CZTI onboard *AstroSat* in its first year of operation. Our study focuses on the application of time-resolved and energy-resolved spectro-polarimetry techniques to obtain detailed polarization information and characterize the emission properties of these GRBs. The primary objective of our study is to delve into the jet compositions of these bright GRBs and constrain the different radiation models of prompt emission. This issue has been a subject of long-

standing debate, and prompt emission spectroscopy on its own has been insufficient to resolve these questions independently.

By exploiting the high-angular-resolution CZTI data, we have derived time-resolved polarization profiles for a sample of GRBs. We studied the $\Gamma\theta_j$ condition to constrain the jet geometry of these bursts, as observed polarization also depends on the jet geometry. We utilized 10.4m GTC and 3.6m DOT telescopes to contain the redshift/ host search of the bursts, which further helps to verify the $\Gamma\theta_j$ condition. Our analysis suggests that the jet emissions from these GRBs were observed on-axis. Furthermore, our comprehensive spectro-polarimetric analysis suggests that GRB 160623A, GRB 160703A, and GRB 160821A have a Poynting flux-dominated jet, and emission could be explained using a thin shell synchrotron emission model in an ordered magnetic field. On the other hand, GRB 160325A and GRB 160802A have the first pulse with a thermal signature followed by non-thermal emission during the second pulse. Our analysis indicates that GRB 160325A and GRB 160802A have a Baryonic dominated jet with mild magnetization. We do not observe any rapid evolution in the polarization angles of GRB 160325A, GRB 160623A, GRB 160703A, and GRB 160802A. However, we observe a rapid change in polarization angle by ~ 90 degrees within the main pulse of very bright GRB 160821A, consistent with our previous results reported in 100-300 keV (Sharma et al. 2019). The profile of GRB 160821A (time-resolved polarization analysis) reveals temporal variations in the angle of polarization, shedding light on the radiation mechanisms and geometry involved in this extreme event. We noted that some authors performed the theoretical simulations and reproduced such large temporal variation in polarization angle under the photospheric emission model. They also discussed the physics and implications of observing such changes (Ito et al. 2024; Parsotan et al. 2020). However, our analysis reveals a hint of high degree of polarization for GRB 160821A, which contrasts with the predictions of the photospheric emission model.

Additionally, we have studied the polarization properties as a function of energy, suggesting a hint of variations in the polarization degree and angle across different energy bands. We noted that the polarization angles of GRB 160325A, GRB 160703A, and GRB 160802A, GRB 160821A obtained for different energy segments remain mostly consistent; however, the polarization angles of GRB 160623A changed with energy (though large associated error due to the limited number of Compton events). Further, we noted that the polarization fraction values have increasing trends with energy, although the

analysis might be limited due to fewer Compton counts in later energy bins. The energy-resolved polarization analysis gives a hint that polarization properties depend on the energy channels of the detectors.

Our results demonstrate the capability of *AstroSat* CZTI for detailed time-resolved and energy-resolved spectro-polarimetry of GRBs. The combination of high-angular-resolution imaging, broad energy coverage, and polarization sensitivity provides a unique opportunity to unravel the complex physics governing these explosive phenomena. By studying the polarization of these GRBs, we obtain important insights into the geometry and magnetic field structures associated with these bursts. Our findings suggest that prompt emission polarization analysis, when combined with spectral and temporal data, possesses a distinct capacity to resolve the long-standing debate surrounding the emission mechanisms of GRBs. A comprehensive analysis that delves into both time-resolved and energy-resolved spectro-polarimetry offers greater insight into the emission mechanisms of GRBs compared to a time-averaged spectro-polarimetric analysis (Gupta 2023).

Our time-resolved and energy-resolved analysis may be somewhat limited due to the relatively low number of Compton events in the finer time/energy bins. We need more observations (extremely bright GRBs with more Compton counts) or more sensitive GRB polarimeters with larger effective areas and refined theoretical models to improve our understanding of the physical processes that drive these energetic and enigmatic events. Additionally, examination of the correlation between spectral parameters and measured polarization parameters for more bright GRBs will provide further constraints on the radiation physics of GRBs. The findings presented in this study pave the way for future investigations and highlight the potential of *AstroSat* CZTI for advancing our understanding of GRBs and their role in the Universe. Further, the insights gained from this study have profound implications for our understanding of high-energy astrophysics and the physical processes associated with GRBs. The scientific community is actively engaged in preparing for the next generation of gamma-ray missions, including COSI, eAstroGAM, AMEGO, AMEGO-X, and POLAR 2. Our research contributes valuable insights for these forthcoming missions, particularly through our time-resolved polarization measurements. This information is instrumental for the development and optimization of upcoming GRB polarimeters such as LEAP, POLAR 2 (Hulsman 2020), COSI, and other missions.

Facilities: AstroSat(CZTI), Fermi(GBM),
Swift(BAT), 10.4m GTC, 3.6m DOT

Software: astropy version 5.1 (Astropy Collaboration et al. 2013, 2018), 3ML version 2.4.0 (Vianello et al. 2015), Fermi GBM Data Tools version 1.1.1.(Goldstein et al. 2022), gtburst version 03-00-00p0, numpy version 1.21.6, matplotlib version 3.3.2

1 We thank the anonymous referee for providing positive and encouraging comments on our manuscript.
2
3 RG and SBP are very grateful to Prof. A. R. Rao for the excellent suggestions and discussion with the project. RG is also thankful to Dr. Tyler Parsotan for reading the manuscript and fruitful discussion. RG, SBP, DB, and VB acknowledge the financial support of ISRO under AstroSat archival Data utilization program (DS.2B-13013(2)/1/2021-Sec.2). This publication uses data from the *AstroSat* mission of the Indian Space Research Organisation (ISRO), archived at the Indian Space Science Data Centre (ISSDC). CZT-Imager is built by a consortium of institutes across India, including the Tata Institute of Fundamental Research (TIFR), Mumbai, the Vikram Sarabhai Space Centre, Thiruvananthapuram, ISRO Satellite Centre (ISAC), Bengaluru, Inter University Centre for Astronomy and Astro-physics, Pune, Physical Research Laboratory, Ahmedabad, Space Application Centre, Ahmedabad. This research also has used data obtained through the HEASARC Online Service, provided by the NASA-GSFC, in support of NASA High Energy Astrophysics Programs. RG was sponsored by the National Aeronautics and Space Administration (NASA) through a contract with ORAU. The views and conclusions contained in this document are those of the authors and should not be interpreted as representing the official policies, either expressed or implied, of the National Aeronautics and Space Administration (NASA) or the U.S. Government. The U.S. Government is authorized to reproduce and distribute reprints for Government purposes notwithstanding any copyright notation herein. AA acknowledges funds and assistance provided by the Council of Scientific & Industrial Research (CSIR), India, under file no. 09/948(0003)/2020-EMR-I. AA also acknowledges the Yushan Young Fellow Program by the Ministry of Education, Taiwan, for financial support. This research is based on observations obtained at the 3.6m Devasthal Optical Telescope (DOT), which is a National Facility run and managed by Aryabhata Research Institute of Observational Sciences (ARIES), an autonomous Institute under the Department of Science and Technology, Government of India.

REFERENCES

- Acuner, Z., Ryde, F., Pe'er, A., Mortlock, D., & Ahlgren, B. 2020, arXiv e-prints, arXiv:2003.06223.
<https://arxiv.org/abs/2003.06223>
- Acuner, Z., Ryde, F., & Yu, H.-F. 2019, MNRAS, 487, 5508, doi: 10.1093/mnras/stz1356
- Ahlgren, B., Larsson, J., Valan, V., et al. 2019, ApJ, 880, 76, doi: 10.3847/1538-4357/ab271b
- Amati, L. 2006, MNRAS, 372, 233, doi: 10.1111/j.1365-2966.2006.10840.x

- Astropy Collaboration, Robitaille, T. P., Tollerud, E. J., et al. 2013, *A&A*, 558, A33, doi: [10.1051/0004-6361/201322068](https://doi.org/10.1051/0004-6361/201322068)
- Astropy Collaboration, Price-Whelan, A. M., Sipőcz, B. M., et al. 2018, *AJ*, 156, 123, doi: [10.3847/1538-3881/aabc4f](https://doi.org/10.3847/1538-3881/aabc4f)
- Atwood, W. B., Abdo, A. A., Ackermann, M., et al. 2009, *ApJ*, 697, 1071, doi: [10.1088/0004-637X/697/2/1071](https://doi.org/10.1088/0004-637X/697/2/1071)
- Axelsson, M., Bissaldi, E., Desiante, R., & Longo, F. 2016, *GRB Coordinates Network*, 19227, 1
- Baring, M. G., & Braby, M. L. 2004, *ApJ*, 613, 460, doi: [10.1086/422867](https://doi.org/10.1086/422867)
- Barthelmy, S. D., Barbier, L. M., Cummings, J. R., et al. 2005, *SSRv*, 120, 143, doi: [10.1007/s11214-005-5096-3](https://doi.org/10.1007/s11214-005-5096-3)
- Beloborodov, A. M. 2017, *ApJ*, 838, 125, doi: [10.3847/1538-4357/aa5c8c](https://doi.org/10.3847/1538-4357/aa5c8c)
- Beloborodov, A. M., & Mészáros, P. 2017, *SSRv*, 207, 87, doi: [10.1007/s11214-017-0348-6](https://doi.org/10.1007/s11214-017-0348-6)
- Bhalerao, V., Kumar, V., Bhattacharya, D., Rao, A. R., & Vadawale, S. 2016a, *GRB Coordinates Network*, 19739, 1
- . 2016b, *GRB Coordinates Network*, 19782, 1
- . 2016c, *GRB Coordinates Network*, 19867, 1
- Bissaldi, E. 2016, *GRB Coordinates Network*, 19754, 1
- Bošnjak, Ž., Barniol Duran, R., & Pe’er, A. 2022, *Galaxies*, 10, 38, doi: [10.3390/galaxies10020038](https://doi.org/10.3390/galaxies10020038)
- Burgess, J. M., Bégué, D., Greiner, J., et al. 2020, *Nature Astronomy*, 4, 174, doi: [10.1038/s41550-019-0911-z](https://doi.org/10.1038/s41550-019-0911-z)
- Burgess, J. M., Kole, M., Berlato, F., et al. 2019, *A&A*, 627, A105, doi: [10.1051/0004-6361/201935056](https://doi.org/10.1051/0004-6361/201935056)
- Caballero-García, M. D., Gupta, R., Pandey, S. B., et al. 2023, *MNRAS*, 519, 3201, doi: [10.1093/mnras/stac3629](https://doi.org/10.1093/mnras/stac3629)
- Castro-Tirado, A. J., Valeev, A. F., Jeong, S., et al. 2016, *GRB Coordinates Network*, 19710, 1
- Cenko, S. B., D’Elia, V., Gehrels, N., et al. 2016, *GRB Coordinates Network*, 19645, 1
- Chand, V., Chattopadhyay, T., Oganessyan, G., et al. 2019, *ApJ*, 874, 70, doi: [10.3847/1538-4357/ab0826](https://doi.org/10.3847/1538-4357/ab0826)
- Chand, V., Chattopadhyay, T., Iyyani, S., et al. 2018, *ApJ*, 862, 154, doi: [10.3847/1538-4357/aacd12](https://doi.org/10.3847/1538-4357/aacd12)
- Chattopadhyay, T. 2021, *Journal of Astrophysics and Astronomy*, 42, 106, doi: [10.1007/s12036-021-09769-5](https://doi.org/10.1007/s12036-021-09769-5)
- Chattopadhyay, T., Vadawale, S. V., Aarthy, E., et al. 2019, *ApJ*, 884, 123, doi: [10.3847/1538-4357/ab40b7](https://doi.org/10.3847/1538-4357/ab40b7)
- Chattopadhyay, T., Gupta, S., Sharma, V., et al. 2021, *arXiv e-prints*, arXiv:2102.13594, <https://arxiv.org/abs/2102.13594>
- Chattopadhyay, T., Gupta, S., Iyyani, S., et al. 2022, *ApJ*, 936, 12, doi: [10.3847/1538-4357/ac82ef](https://doi.org/10.3847/1538-4357/ac82ef)
- Chen, W. J., Urata, Y., Huang, K., et al. 2020, *ApJL*, 891, L15, doi: [10.3847/2041-8213/ab76d4](https://doi.org/10.3847/2041-8213/ab76d4)
- Coburn, W., & Boggs, S. E. 2003, *Nature*, 423, 415, doi: [10.1038/nature01612](https://doi.org/10.1038/nature01612)
- D’Elia, V., Izzo, L., Malesani, D., et al. 2016, *GRB Coordinates Network*, 19655, 1
- Eichler, D., & Levinson, A. 2004, *ApJL*, 614, L13, doi: [10.1086/425310](https://doi.org/10.1086/425310)
- Fan, Y.-Z., Wei, D.-M., Zhang, F.-W., & Zhang, B.-B. 2012, *ApJL*, 755, L6, doi: [10.1088/2041-8205/755/1/L6](https://doi.org/10.1088/2041-8205/755/1/L6)
- Frail, D. A., Kulkarni, S. R., Sari, R., et al. 2001, *ApJL*, 562, L55, doi: [10.1086/338119](https://doi.org/10.1086/338119)
- Frederiks, D., Golenetskii, S., Aptekar, R., et al. 2016a, *GRB Coordinates Network*, 19554, 1
- . 2016b, *GRB Coordinates Network*, 19649, 1
- Ghirlanda, G., Nappo, F., Ghisellini, G., et al. 2018, *A&A*, 609, A112, doi: [10.1051/0004-6361/201731598](https://doi.org/10.1051/0004-6361/201731598)
- Gill, R., Granot, J., & Kumar, P. 2020, *MNRAS*, 491, 3343, doi: [10.1093/mnras/stz2976](https://doi.org/10.1093/mnras/stz2976)
- Gill, R., Kole, M., & Granot, J. 2021, *Galaxies*, 9, 82, doi: [10.3390/galaxies9040082](https://doi.org/10.3390/galaxies9040082)
- Goldstein, A., Cleveland, W. H., & Kocevski, D. 2022, *Fermi GBM Data Tools: v1.1.1*, <https://fermi.gsfc.nasa.gov/ssc/data/analysis/gbm>
- Granot, J., Piran, T., & Sari, R. 2000, *ApJL*, 534, L163, doi: [10.1086/312661](https://doi.org/10.1086/312661)
- Gupta, R. 2023, *arXiv e-prints*, arXiv:2312.16265, doi: [10.48550/arXiv.2312.16265](https://doi.org/10.48550/arXiv.2312.16265)
- Gupta, R., Pandey, S. B., Ror, A. K., Aryan, A., & Tiwari, S. N. 2023, *arXiv e-prints*, arXiv:2307.15585, doi: [10.48550/arXiv.2307.15585](https://doi.org/10.48550/arXiv.2307.15585)
- Gupta, R., Oates, S. R., Pandey, S. B., et al. 2021, *MNRAS*, 505, 4086, doi: [10.1093/mnras/stab1573](https://doi.org/10.1093/mnras/stab1573)
- Gupta, R., Gupta, S., Chattopadhyay, T., et al. 2022a, *MNRAS*, 511, 1694, doi: [10.1093/mnras/stac015](https://doi.org/10.1093/mnras/stac015)
- Gupta, R., Pandey, S. B., Kumar, A., et al. 2022b, *Journal of Astrophysics and Astronomy*, 43, 82, doi: [10.1007/s12036-022-09865-0](https://doi.org/10.1007/s12036-022-09865-0)
- Gupta, R., Kumar, A., Pandey, S. B., et al. 2022c, *Journal of Astrophysics and Astronomy*, 43, 11, doi: [10.1007/s12036-021-09794-4](https://doi.org/10.1007/s12036-021-09794-4)
- Hagen, L. M. Z., & Cenko, S. B. 2016, *GRB Coordinates Network*, 19656, 1
- Hulsman, J. 2020, in *Society of Photo-Optical Instrumentation Engineers (SPIE) Conference Series*, Vol. 11444, *Space Telescopes and Instrumentation 2020: Ultraviolet to Gamma Ray*, ed. J.-W. A. den Herder, S. Nikzad, & K. Nakazawa, 114442V, doi: [10.1117/12.2559374](https://doi.org/10.1117/12.2559374)
- Ito, H., Matsumoto, J., Nagataki, S., et al. 2019, *Nature Communications*, 10, 1504, doi: [10.1038/s41467-019-09281-z](https://doi.org/10.1038/s41467-019-09281-z)

- . 2024, *ApJ*, 961, 243, doi: [10.3847/1538-4357/ace775](https://doi.org/10.3847/1538-4357/ace775)
- Iyyani, S. 2022, *Journal of Astrophysics and Astronomy*, 43, 37, doi: [10.1007/s12036-022-09817-8](https://doi.org/10.1007/s12036-022-09817-8)
- Iyyani, S., Ryde, F., Burgess, J. M., Pe'er, A., & Bégué, D. 2016, *MNRAS*, 456, 2157, doi: [10.1093/mnras/stv2751](https://doi.org/10.1093/mnras/stv2751)
- Kalemci, E., Boggs, S. E., Kouveliotou, C., Finger, M., & Baring, M. G. 2007, *ApJS*, 169, 75, doi: [10.1086/510676](https://doi.org/10.1086/510676)
- Kole, M., De Angelis, N., Berlato, F., et al. 2020, *A&A*, 644, A124, doi: [10.1051/0004-6361/202037915](https://doi.org/10.1051/0004-6361/202037915)
- Kozlova, A., Golenetskii, S., Aptekar, R., et al. 2016a, GRB Coordinates Network, 19767, 1
- . 2016b, GRB Coordinates Network, 19842, 1
- Kumar, P., & Zhang, B. 2015, *PhR*, 561, 1, doi: [10.1016/j.physrep.2014.09.008](https://doi.org/10.1016/j.physrep.2014.09.008)
- Levinson, A., & Eichler, D. 2005, *ApJL*, 629, L13, doi: [10.1086/444356](https://doi.org/10.1086/444356)
- Liang, E.-W., Yi, S.-X., Zhang, J., et al. 2010, *ApJ*, 725, 2209, doi: [10.1088/0004-637X/725/2/2209](https://doi.org/10.1088/0004-637X/725/2/2209)
- Lien, A. Y., Barthelmy, S. D., Cenko, S. B., et al. 2016, GRB Coordinates Network, 19648, 1
- Lundman, C., Pe'er, A., & Ryde, F. 2013, *MNRAS*, 428, 2430, doi: [10.1093/mnras/sts219](https://doi.org/10.1093/mnras/sts219)
- Mailyan, B., Toelge, K., & Roberts, O. 2016, GRB Coordinates Network, 19555, 1
- Malesani, D., de Ugarte Postigo, A., de Pasquale, M., et al. 2016, GRB Coordinates Network, 19708, 1
- Marrocchesi, P. S., Yoshida, A., Sakamoto, T., et al. 2016, GRB Coordinates Network, 19865, 1
- McConnell, M. L. 2017, *NewAR*, 76, 1, doi: [10.1016/j.newar.2016.11.001](https://doi.org/10.1016/j.newar.2016.11.001)
- McEney, J., Racusin, J., & Longo, F. 2016, GRB Coordinates Network, 19831, 1
- McGlynn, S., Clark, D. J., Dean, A. J., et al. 2007, *A&A*, 466, 895, doi: [10.1051/0004-6361:20066179](https://doi.org/10.1051/0004-6361:20066179)
- Meegan, C., Lichti, G., Bhat, P. N., et al. 2009, *ApJ*, 702, 791, doi: [10.1088/0004-637X/702/1/791](https://doi.org/10.1088/0004-637X/702/1/791)
- Minaev, P. Y., & Pozanenko, A. S. 2020, *MNRAS*, 492, 1919, doi: [10.1093/mnras/stz3611](https://doi.org/10.1093/mnras/stz3611)
- Mingo, B., Beardmore, A. P., D'Ai, A., et al. 2016, GRB Coordinates Network, 19558, 1
- Nava, L., Salvaterra, R., Ghirlanda, G., et al. 2012, *MNRAS*, 421, 1256, doi: [10.1111/j.1365-2966.2011.20394.x](https://doi.org/10.1111/j.1365-2966.2011.20394.x)
- Nayana, A. J., Chandra, P., Rao, A. R., Bhattacharya, D., & Bhalerao, V. 2016, GRB Coordinates Network, 19849, 1
- Oganesyan, G., Nava, L., Ghirlanda, G., & Celotti, A. 2017, *ApJ*, 846, 137, doi: [10.3847/1538-4357/aa831e](https://doi.org/10.3847/1538-4357/aa831e)
- . 2018, *A&A*, 616, A138, doi: [10.1051/0004-6361/201732172](https://doi.org/10.1051/0004-6361/201732172)
- Oganesyan, G., Nava, L., Ghirlanda, G., Melandri, A., & Celotti, A. 2019, *A&A*, 628, A59, doi: [10.1051/0004-6361/201935766](https://doi.org/10.1051/0004-6361/201935766)
- Panasyuk, M. I., Svertilov, S. I., Bogomolov, V. V., et al. 2016, GRB Coordinates Network, 19759, 1
- Pandey, S. B. 2016, in *Revista Mexicana de Astronomia y Astrofisica Conference Series*, Vol. 48, *Revista Mexicana de Astronomia y Astrofisica Conference Series*, 83–88
- Pandey, S. B., Yadav, R. K. S., Nanjappa, N., et al. 2018, *Bulletin de la Societe Royale des Sciences de Liege*, 87, 42
- Pandey, S. B., Kumar, A., Reddy, B. K., et al. 2023, *Journal of Astronomical Instrumentation*, 12, 2240009, doi: [10.1142/S2251171722400098](https://doi.org/10.1142/S2251171722400098)
- Parsotan, T., & Ito, H. 2022, *Universe*, 8, 310, doi: [10.3390/universe8060310](https://doi.org/10.3390/universe8060310)
- Parsotan, T., & Lazzati, D. 2022, *ApJ*, 926, 104, doi: [10.3847/1538-4357/ac4093](https://doi.org/10.3847/1538-4357/ac4093)
- Parsotan, T., López-Cámara, D., & Lazzati, D. 2020, *ApJ*, 896, 139, doi: [10.3847/1538-4357/ab910f](https://doi.org/10.3847/1538-4357/ab910f)
- Pe'er, A. 2015, *Advances in Astronomy*, 2015, 907321, doi: [10.1155/2015/907321](https://doi.org/10.1155/2015/907321)
- Pe'Er, A., & Ryde, F. 2017, *International Journal of Modern Physics D*, 26, 1730018, doi: [10.1142/S021827181730018X](https://doi.org/10.1142/S021827181730018X)
- Pintore, F., Tiengo, A., Mereghetti, S., et al. 2017, *MNRAS*, 472, 1465, doi: [10.1093/mnras/stx2062](https://doi.org/10.1093/mnras/stx2062)
- Piran, T. 2004, *Reviews of Modern Physics*, 76, 1143, doi: [10.1103/RevModPhys.76.1143](https://doi.org/10.1103/RevModPhys.76.1143)
- Preece, R. D., Briggs, M. S., Mallozzi, R. S., et al. 1998, *ApJL*, 506, L23, doi: [10.1086/311644](https://doi.org/10.1086/311644)
- Rao, A. R., Chand, V., Hingar, M. K., et al. 2016, *ApJ*, 833, 86, doi: [10.3847/1538-4357/833/1/86](https://doi.org/10.3847/1538-4357/833/1/86)
- Ratheesh, A., Rao, A. R., Mithun, N. P. S., et al. 2021, *Journal of Astrophysics and Astronomy*, 42, 37, doi: [10.1007/s12036-021-09716-4](https://doi.org/10.1007/s12036-021-09716-4)
- Ravasio, M. E., Ghirlanda, G., Nava, L., & Ghisellini, G. 2019, *A&A*, 625, A60, doi: [10.1051/0004-6361/201834987](https://doi.org/10.1051/0004-6361/201834987)
- Ravasio, M. E., Oganesyan, G., Ghirlanda, G., et al. 2018, *A&A*, 613, A16, doi: [10.1051/0004-6361/201732245](https://doi.org/10.1051/0004-6361/201732245)
- Rees, M. J., & Mészáros, P. 2005, *ApJ*, 628, 847, doi: [10.1086/430818](https://doi.org/10.1086/430818)
- Roberts, O. J. 2016, GRB Coordinates Network, 19224, 1
- Rutledge, R. E., & Fox, D. B. 2004, *MNRAS*, 350, 1288, doi: [10.1111/j.1365-2966.2004.07665.x](https://doi.org/10.1111/j.1365-2966.2004.07665.x)
- Ryde, F., Pe'er, A., Nymark, T., et al. 2011, *MNRAS*, 415, 3693, doi: [10.1111/j.1365-2966.2011.18985.x](https://doi.org/10.1111/j.1365-2966.2011.18985.x)
- Sharma, S., Ojha, D. K., Ghosh, A., et al. 2022, *PASP*, 134, 085002, doi: [10.1088/1538-3873/ac81eb](https://doi.org/10.1088/1538-3873/ac81eb)
- Sharma, V., Iyyani, S., & Bhattacharya, D. 2021, *ApJL*, 908, L2, doi: [10.3847/2041-8213/abd53f](https://doi.org/10.3847/2041-8213/abd53f)

- Sharma, V., Iyyani, S., Bhattacharya, D., et al. 2020, MNRAS, 493, 5218, doi: [10.1093/mnras/staa570](https://doi.org/10.1093/mnras/staa570)
- . 2019, ApJL, 882, L10, doi: [10.3847/2041-8213/ab3a48](https://doi.org/10.3847/2041-8213/ab3a48)
- Siegel, M. H., Barthelmy, S. D., Lien, A. Y., Page, K. L., & Palmer, D. M. 2016, GRB Coordinates Network, 19830, 1
- Sonbas, E., Lien, A. Y., & Page, K. L. 2016, GRB Coordinates Network, 19222, 1
- Stanbro, M., & Meegan, C. 2016, GRB Coordinates Network, 19835, 1
- Tamura, T., Yoshida, A., Sakamoto, T., et al. 2016, GRB Coordinates Network, 19778, 1
- Tavani, M. 1996, ApJ, 466, 768, doi: [10.1086/177551](https://doi.org/10.1086/177551)
- Tiengo, A., Vianello, G., Esposito, P., & Salvaterra, R. 2016, GRB Coordinates Network, 19559, 1
- Toma, K. 2013, ArXiv e-prints.
<https://arxiv.org/abs/1308.5733>
- Toma, K., Sakamoto, T., Zhang, B., et al. 2009, ApJ, 698, 1042, doi: [10.1088/0004-637X/698/2/1042](https://doi.org/10.1088/0004-637X/698/2/1042)
- Tsvetkova, A., Golenetskii, S., Aptekar, R., et al. 2016, GRB Coordinates Network, 19244, 1
- Tsvetkova, A., Frederiks, D., Golenetskii, S., et al. 2017, ApJ, 850, 161, doi: [10.3847/1538-4357/aa96af](https://doi.org/10.3847/1538-4357/aa96af)
- Uhm, Z. L., & Zhang, B. 2014, Nature Physics, 10, 351, doi: [10.1038/nphys2932](https://doi.org/10.1038/nphys2932)
- Vadawale, S. V., Chattopadhyay, T., Mithun, N. P. S., et al. 2018, Nature Astronomy, 2, 50, doi: [10.1038/s41550-017-0293-z](https://doi.org/10.1038/s41550-017-0293-z)
- Vaishnava, C. S., Mithun, N. P. S., Vadawale, S. V., et al. 2022, Journal of Astronomical Telescopes, Instruments, and Systems, 8, 038005, doi: [10.1117/1.JATIS.8.3.038005](https://doi.org/10.1117/1.JATIS.8.3.038005)
- Vianello, G., Dirirsa, F., Omodei, N., et al. 2016, GRB Coordinates Network, 19553, 1
- Vianello, G., Lauer, R. J., Younk, P., et al. 2015, arXiv e-prints, arXiv:1507.08343.
<https://arxiv.org/abs/1507.08343>
- Willis, D. R., Barlow, E. J., Bird, A. J., et al. 2005, A&A, 439, 245, doi: [10.1051/0004-6361:20052693](https://doi.org/10.1051/0004-6361:20052693)
- Yamaoka, K., Yoshida, A., Sakamoto, T., et al. 2016, GRB Coordinates Network, 19597, 1
- Yamazaki, R., Ioka, K., & Nakamura, T. 2004, ApJL, 606, L33, doi: [10.1086/421084](https://doi.org/10.1086/421084)
- Yonetoku, D., Murakami, T., Tsutsui, R., et al. 2010, PASJ, 62, 1495, doi: [10.1093/pasj/62.6.1495](https://doi.org/10.1093/pasj/62.6.1495)
- Yonetoku, D., Murakami, T., Gunji, S., et al. 2011a, ApJL, 743, L30, doi: [10.1088/2041-8205/743/2/L30](https://doi.org/10.1088/2041-8205/743/2/L30)
- . 2011b, PASJ, 63, 625, doi: [10.1093/pasj/63.3.625](https://doi.org/10.1093/pasj/63.3.625)
- . 2012, ApJL, 758, L1, doi: [10.1088/2041-8205/758/1/L1](https://doi.org/10.1088/2041-8205/758/1/L1)
- Zhang, B. 2011, Comptes Rendus Physique, 12, 206, doi: [10.1016/j.crhy.2011.03.004](https://doi.org/10.1016/j.crhy.2011.03.004)
- . 2020, Nature Astronomy, 4, 210, doi: [10.1038/s41550-020-1041-3](https://doi.org/10.1038/s41550-020-1041-3)

APPENDIX

A. FIGURES

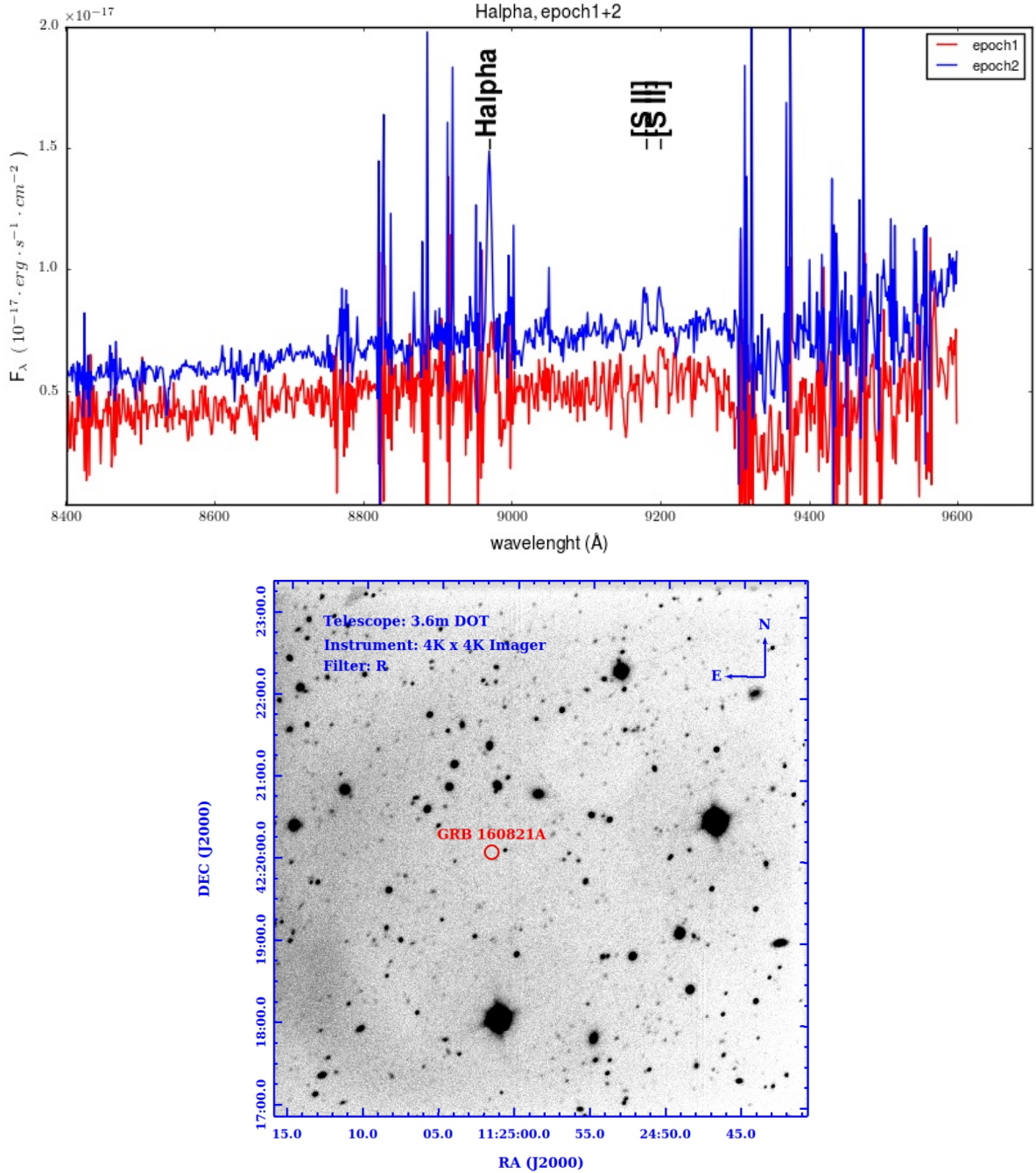


Figure A1. Our efforts to constrain the redshift of the GRBs using larger optical telescopes. Top: Redshift measurement ($z = 0.367$) of GRB 160623A using 10.4m GTC observations. Our analysis revealed emission lines of H-alpha and [SII] at a common redshift of $z = 0.367$. Bottom: R-filter stacked image of the field of GRB 160821A taken using 3.6m DOT/4K×4K IMAGER (Pandey et al. 2018). The red circle marks the associated uncertainties in the position of the burst.

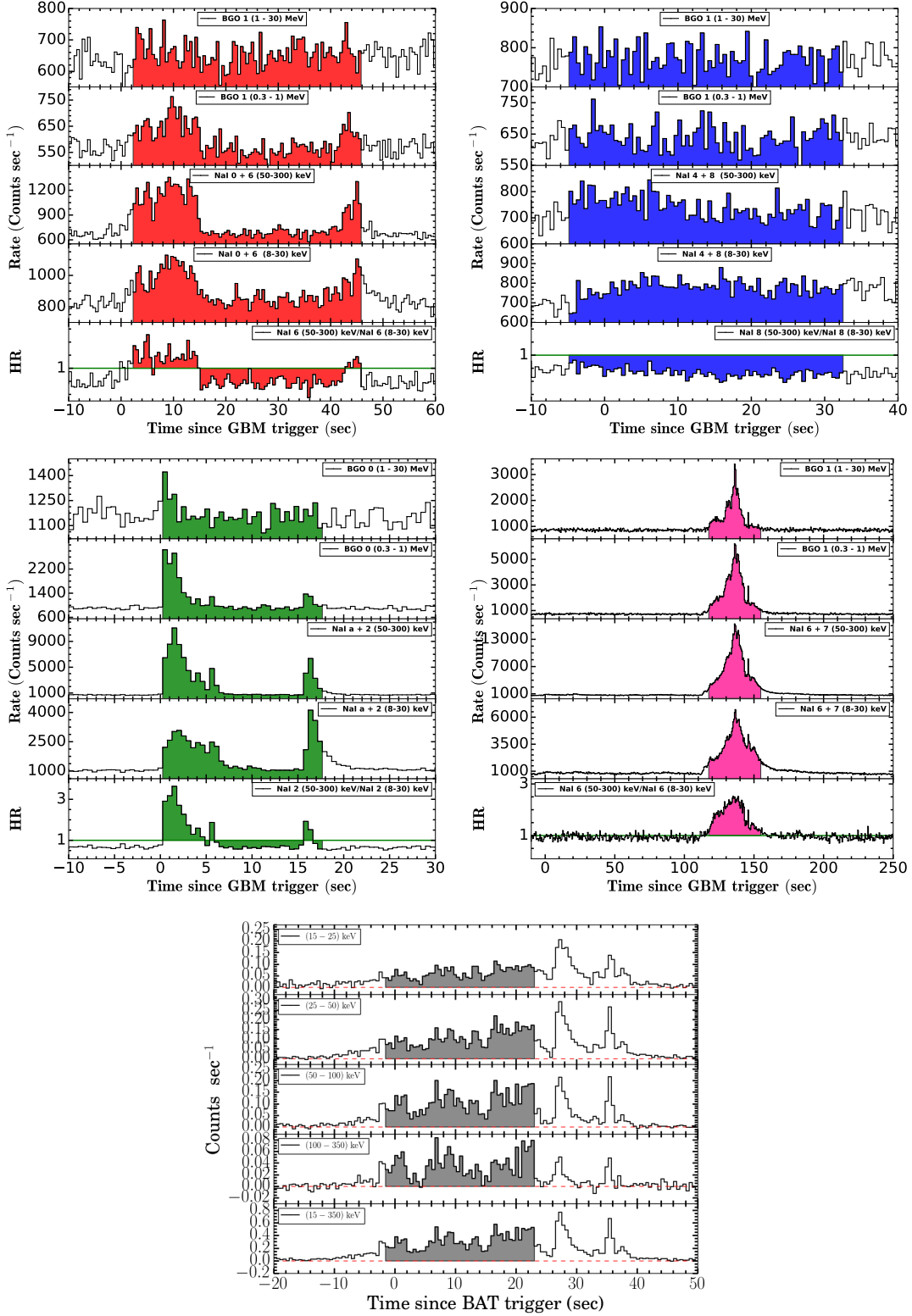


Figure A2. Multi-channels light curve profiles of *Fermi* detected (GRB 160325A (top-left), GRB 160623A (top-right), GRB 160802A (middle-left), and GRB 160821A (middle-right)) and *Swift* detected (GRB 160703A, bottom) GRBs in our sample. The HR (50-300 keV/8-30 keV) evolution for *Fermi* GRBs is shown in the bottom sub-panels of each GRBs. The shaded colored regions correspond to the time interval used for the time-integrated spectro-polarimetric analysis.

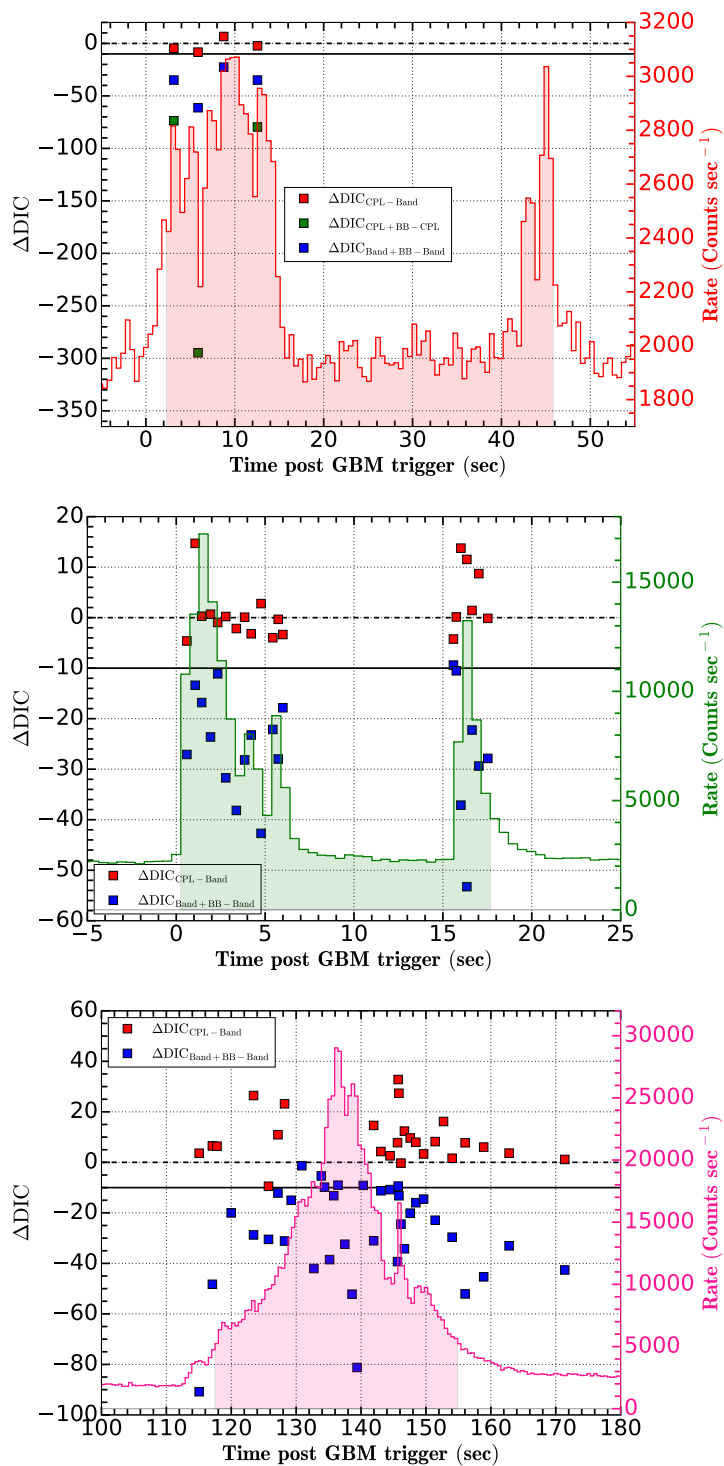


Figure A3. The selection of the best-fit model using the difference of deviance information criterion values obtained from different models. The horizontal black dashed and solid lines demonstrate ΔDIC corresponding to zero and -10, respectively. The top, middle, and bottom panels illustrate the difference in DIC values for GRB 160325A, GRB 160802A, and GRB 160821A, respectively.

B. TABLES

Table B1. Empirical and physical spectral fitting of the time-averaged spectrum of GRBs of our sample. Time-integrated flux has been calculated from 10 keV to 40 MeV energy range. For the *Swift* detected GRB 160703A, the time-integrated flux has been calculated from 15 keV to 150 keV energy range.

Spectral model	Spectral parameters					Statistics		
GRB 160325A								
	α_{pt}	E_p/E_c (keV)	β_{pt}	kT_{BB} (keV)	Flux (erg/cm ² /sec)	DIC	Δ DIC	
Band	$-0.79^{+0.07}_{-0.07}$	$228.54^{+21.76}_{-21.69}$	$-2.60^{+0.27}_{-0.28}$	-	5.28×10^{-07}	5300.69	-	
Band+BB	$-0.78^{+0.07}_{-0.07}$	$227.57^{+21.04}_{-21.34}$	$-2.53^{+0.24}_{-0.24}$	$11.84^{+7.44}_{-7.56}$	5.52×10^{-07}	5289.52	-11.17	
CPL	$-0.83^{+0.06}_{-0.06}$	$215.12^{+27.30}_{-26.87}$	-	-	4.05×10^{-07}	5303.23	-	
CPL+BB	$-0.83^{+0.06}_{-0.06}$	$216.69^{+26.33}_{-26.25}$	-	$12.07^{+7.66}_{-7.74}$	4.07×10^{-07}	5291.95	-11.28	
bkn2pow	$\alpha_{1,2,3} = 0.80^{+0.17}_{-0.18}, 1.24^{+0.07}_{-0.07}, 2.51^{+0.20}_{-0.19}$		$E_{b1,b2} = 39.64^{+10.04}_{-9.23}, 187.81^{+21.53}_{-20.98}$		5.26×10^{-07}	5250.34	-	
Synchrotron	B (G)	p	γ_{cool}	-	Flux (erg/cm ² /sec)	DIC	Δ DIC	
	$1.74^{+0.25}_{-0.25}$	$4.44^{+0.79}_{-0.73}$	$652059.43^{+208969.3}_{-193485.70}$	-	4.77×10^{-07}	5299.18	-	
GRB 160623A								
PL	$-1.63^{+0.04}_{-0.04}$	-	-	-	5.88×10^{-07}	4682.24	-	
Band	$-1.34^{+0.10}_{-0.10}$	$209.32^{+70.68}_{-70.50}$	$-2.37^{+0.42}_{-0.43}$	-	1.67×10^{-07}	4674.55	-	
Band+BB	$-1.34^{+0.10}_{-0.10}$	$205.36^{+66.88}_{-67.00}$	$-2.36^{+0.43}_{-0.43}$	$11.01^{+6.57}_{-6.76}$	1.66×10^{-07}	4664.81	-9.74	
CPL	$-1.31^{+0.08}_{-0.08}$	$268.34^{+69.62}_{-68.68}$	-	-	9.71×10^{-08}	4680.49	-	
CPL+BB	$-0.85^{+0.20}_{-0.20}$	$235.72^{+64.05}_{-62.56}$	-	$7.24^{+0.92}_{-0.96}$	1.12×10^{-07}	4634.69	-45.80	
bkn2pow	$\alpha_{1,2,3} = 0.97^{+0.28}_{-0.29}, 1.72^{+0.09}_{-0.09}, 2.18^{+0.34}_{-0.33}$		$E_{b1,b2} = 27.72^{+6.45}_{-6.39}, 240.32^{+72.73}_{-73.44}$		2.03×10^{-07}	4629.71	-	
Synchrotron	B (G)	p	γ_{cool}	-	Flux (erg/cm ² /sec)	DIC	Δ DIC	
	$1.28^{+0.37}_{-0.37}$	$2.40^{+0.29}_{-0.28}$	$464821.58^{+232032.08}_{-202812.12}$	-	1.99×10^{-07}	4665.72	-	
GRB 160703A								
PL	$-1.06^{+0.02}_{-0.01}$	-	-	-	2.32×10^{-07}	65.46	-	
CPL	$-0.89^{+0.03}_{-0.03}$	$332.46^{+60.56}_{-59.20}$	-	-	2.29×10^{-07}	66.48	-	
GRB 160802A								
Band	$-0.66^{+0.02}_{-0.02}$	$279.43^{+8.57}_{-8.47}$	$-2.50^{+0.09}_{-0.09}$	-	5.05×10^{-06}	4945.18	-	
Band+BB	$-0.78^{+0.04}_{-0.04}$	$363.97^{+29.57}_{-31.32}$	$-2.89^{+0.25}_{-0.25}$	$27.42^{+2.52}_{-2.54}$	4.62×10^{-06}	4924.29	-20.89	
CPL	$-0.73^{+0.02}_{-0.02}$	$250.52^{+8.14}_{-7.94}$	-	-	3.73×10^{-06}	4975.17	-	
CPL+BB	$-0.83^{+0.03}_{-0.03}$	$348.03^{+25.46}_{-25.51}$	-	$28.69^{+1.93}_{-1.93}$	4.00×10^{-06}	4923.32	-51.85	
bkn2pow	$\alpha_{1,2,3} = 0.82^{+0.02}_{-0.02}, 1.49^{+0.04}_{-0.04}, 2.54^{+0.08}_{-0.08}$		$E_{b1,b2} = 89.02^{+3.67}_{-3.66}, 310.01^{+20.99}_{-21.36}$		4.99×10^{-06}	4956.84	-	
Synchrotron	B (G)	p	γ_{cool}	-	Flux (erg/cm ² /sec)	DIC	Δ DIC	
	$1.78^{+0.14}_{-0.14}$	$5.42^{+0.35}_{-0.36}$	$6219994.0^{+1971658.0}_{-1971658.0}$	-	4.27×10^{-06}	1280.03	-	
GRB 160821A								
Band	$-0.96^{+0.01}_{-0.01}$	$941.35^{+13.75}_{-14.02}$	$-2.30^{+0.02}_{-0.02}$	-	3.12×10^{-05}	6689.98	-	
Band+BB	$-0.97^{+0.01}_{-0.01}$	$1047.37^{+21.83}_{-21.64}$	$-2.35^{+0.02}_{-0.02}$	$30.01^{+2.13}_{-2.09}$	3.12×10^{-05}	6598.74	-91.24	
CPL	$-1.02^{+0.01}_{-0.01}$	$1302.86^{+19.23}_{-18.84}$	-	-	2.50×10^{-05}	7892.62	-	
CPL+BB	$-1.08^{+0.01}_{-0.01}$	$1889.09^{+37.24}_{-36.73}$	-	$56.85^{+1.75}_{-1.72}$	2.76×10^{-05}	7237.90	-654.72	
bkn2pow	$\alpha_{1,2,3} = 0.95^{+0.01}_{-0.01}, 1.29^{+0.01}_{-0.01}, 2.27^{+0.01}_{-0.01}$		$E_{b1,b2} = 101.88^{+1.64}_{-1.61}, 744.43^{+17.99}_{-16.61}$		3.19×10^{-05}	6757.77	-	
Synchrotron	B (G)	p	γ_{cool}	-	Flux (erg/cm ² /sec)	DIC	Δ DIC	
	$1.91^{+0.03}_{-0.03}$	$2.53^{+0.02}_{-0.02}$	$201407.60^{+1190.84}_{-1180.38}$	-	3.30×10^{-05}	7340.93	-	

Table B2. The time-resolved spectral analysis of GRB 160325A was conducted using empirical models, namely the **Cutoff power-law** and **CPL + Blackbody**. The flux values (in $\text{erg cm}^{-2} \text{s}^{-1}$) reported in this study were calculated within the energy range of 8 keV to 40 MeV.

T_{start} (s)	T_{stop} (s)	CPL			CPL+BB				CPL DIC	CPL+BB DIC	Δ DIC
		Γ	E_c (keV)	Flux $\times 10^{-06}$	Γ	E_c (keV)	kT (keV)	Flux $\times 10^{-06}$			
1.605	4.684	$-0.55_{-0.10}^{0.11}$	$186.13_{-28.91}^{28.38}$	0.92	$-0.54_{-0.11}^{0.10}$	$188.44_{-29.25}^{28.93}$	$11.92_{-7.85}^{8.27}$	0.92	2008.58	1934.9	-73.68
4.817	6.911	$-0.56_{-0.14}^{0.14}$	$146.97_{-28.41}^{28.42}$	0.75	$-0.56_{-0.14}^{0.14}$	$151.78_{-31.42}^{29.47}$	$11.97_{-8.24}^{8.40}$	0.75	1610.44	1315.75	-294.69
6.911	10.594	$-0.88_{-0.05}^{0.05}$	$292.80_{-36.06}^{34.77}$	1.5	$-0.87_{-0.06}^{0.06}$	$293.82_{-37.04}^{37.76}$	$12.20_{-7.53}^{7.13}$	1.48	2289.79	-14.76	-2304.55
10.594	14.505	$-0.71_{-0.07}^{0.07}$	$234.40_{-28.46}^{28.28}$	1.19	$-0.65_{-0.11}^{0.11}$	$223.32_{-33.18}^{31.92}$	$9.85_{-5.31}^{5.97}$	1.13	2361.18	2281.56	-79.62
44.13	45.471	$-0.67_{-0.12}^{0.12}$	$162.67_{-30.15}^{29.99}$	0.98	$-0.67_{-0.13}^{0.13}$	$164.65_{-31.46}^{31.41}$	$11.41_{-7.86}^{8.27}$	0.97	1130.91	772.52	-358.39

Table B3. The time-resolved spectral analysis of GRB 160325A was conducted using empirical models, namely the **Band** and **Band + Blackbody**. The flux values (in $\text{erg cm}^{-2} \text{s}^{-1}$) reported in this study were calculated within the energy range of 8 keV to 40 MeV.

T_{start} (s)	T_{stop} (s)	α_{pt}	β_{pt}	E_p (keV)	Flux $\times 10^{-06}$	α_{pt}	β_{pt}	E_p (keV)	kT (keV)	Flux $\times 10^{-06}$	DIC _{Band}	DIC _{Band+BB}	Δ DIC
1.605	4.684	$-0.46_{-0.12}^{0.12}$	$-2.59_{-0.29}^{0.29}$	$235.52_{-26.46}^{26.64}$	1.26	$-0.45_{-0.13}^{0.13}$	$-2.63_{-0.30}^{0.30}$	$237.82_{-27.80}^{26.83}$	$11.01_{-7.17}^{7.56}$	1.24	2013.13	1978.2	-34.93
4.817	6.911	$-0.48_{-0.16}^{0.16}$	$-2.62_{-0.31}^{0.31}$	$186.38_{-23.78}^{24.09}$	1.01	$-0.49_{-0.16}^{0.16}$	$-2.65_{-0.31}^{0.31}$	$192.18_{-26.16}^{25.30}$	$11.95_{-8.02}^{8.68}$	1.0	1618.76	1557.52	-61.24
6.911	10.594	$-0.79_{-0.08}^{0.08}$	$-2.28_{-0.21}^{0.21}$	$260.82_{-34.79}^{35.33}$	2.38	$-0.77_{-0.09}^{0.09}$	$-2.31_{-0.21}^{0.21}$	$265.08_{-35.89}^{35.73}$	$11.02_{-6.60}^{6.72}$	2.3	2283.19	2260.57	-22.62
10.594	14.505	$-0.69_{-0.08}^{0.07}$	$-2.78_{-0.29}^{0.29}$	$279.91_{-24.44}^{24.56}$	1.46	$-0.57_{-0.17}^{0.21}$	$-2.84_{-0.30}^{0.30}$	$274.81_{-24.57}^{24.86}$	$9.55_{-4.63}^{5.27}$	1.42	2363.46	2328.57	-34.89
44.13	45.471	$-0.63_{-0.13}^{0.13}$	$-2.81_{-0.31}^{0.32}$	$198.19_{-23.51}^{23.17}$	1.22	$-0.62_{-0.14}^{0.14}$	$-2.85_{-0.32}^{0.33}$	$200.19_{-24.16}^{23.66}$	$11.26_{-7.48}^{7.81}$	1.21	1137.76	1079.9	-57.86

Table B4. The time-resolved spectral analysis of GRB 160325A was conducted using physical model, namely the **Synchrotron**. The flux values (in $\text{erg cm}^{-2} \text{s}^{-1}$) reported in this study were calculated within the energy range of 8 keV to 40 MeV.

T_{start} (s)	T_{stop} (s)	Synchrotron				DIC	Δ DIC
		B (G)	p	$\gamma_{\text{cool}} \times 10^4$ (keV)	Flux ($\times 10^{-06}$)		
1.605	4.684	$2.24_{-0.33}^{0.33}$	$4.90_{-0.74}^{0.72}$	$278.36_{-211.47}^{295.90}$	1.18	2017.57	-82.67
4.817	6.911	$1.64_{-0.28}^{0.28}$	$4.81_{-0.77}^{0.78}$	$295.88_{-228.85}^{301.89}$	0.94	1623.3	-307.55
6.911	10.594	$1.57_{-0.28}^{0.29}$	$3.69_{-0.52}^{0.53}$	$254.06_{-193.23}^{248.57}$	2.07	2275.61	-15.04
10.594	14.505	$2.28_{-0.29}^{0.30}$	$5.09_{-0.62}^{0.60}$	$247.48_{-186.56}^{221.99}$	1.4	2356.47	-74.91
44.13	45.471	$1.60_{-0.24}^{0.25}$	$5.01_{-0.71}^{0.69}$	$269.59_{-204.95}^{259.69}$	1.18	1137.83	-365.31

Table B5. Similar to B2 but for GRB 160802A.

T_{start} (s)	T_{stop} (s)	CPL			CPL+BB				CPL DIC	CPL+BB DIC	Δ DIC
		Γ	E_c (keV)	Flux $\times 10^{-06}$	Γ	E_c (keV)	kT (keV)	Flux $\times 10^{-06}$			
0.238	0.962	-0.39 ^{0.03} _{-0.03}	319.54 ^{15.39} _{-15.87}	21.5	-0.38 ^{0.04} _{-0.04}	324.64 ^{19.40} _{-18.78}	18.25 ^{12.56} _{-12.54}	21.4	1542.86	557.25	-985.61
0.962	1.171	-0.23 ^{0.05} _{-0.05}	221.61 ^{14.89} _{-14.64}	26.0	-0.21 ^{0.05} _{-0.05}	227.45 ^{18.46} _{-17.96}	18.65 ^{12.27} _{-12.43}	25.7	286.19	237.36	-48.83
1.171	1.695	-0.30 ^{0.03} _{-0.04}	215.94 ^{9.94} _{-9.73}	20.8	-0.28 ^{0.06} _{-0.06}	244.00 ^{17.99} _{-17.81}	28.98 ^{3.40} _{-3.26}	20.1	1211.21	1180.81	-30.4
1.695	2.16	-0.29 ^{0.05} _{-0.05}	158.19 ^{9.01} _{-9.11}	12.2	-0.30 ^{0.06} _{-0.05}	163.54 ^{10.40} _{-13.34}	15.28 ^{12.61} _{-10.63}	12.3	958.5	929.28	-29.22
2.16	2.504	-0.35 ^{0.06} _{-0.06}	147.31 ^{11.13} _{-10.87}	8.66	-0.34 ^{0.07} _{-0.07}	148.92 ^{12.65} _{-12.46}	13.62 ^{8.08} _{-8.88}	8.6	620.06	414.34	-205.72
2.504	3.065	-0.51 ^{0.06} _{-0.06}	142.84 ^{12.41} _{-12.29}	5.6	-0.59 ^{0.12} _{-0.15}	170.79 ^{47.23} _{-34.89}	18.37 ^{10.21} _{-12.04}	6.01	1104.79	644.97	-459.82
3.065	3.695	-0.63 ^{0.08} _{-0.08}	127.41 ^{14.74} _{-14.59}	2.83	-0.65 ^{0.09} _{-0.10}	137.96 ^{20.17} _{-21.79}	14.07 ^{7.49} _{-8.71}	2.8	1098.42	1070.04	-28.38
3.695	4.001	-0.60 ^{0.07} _{-0.07}	189.71 ^{21.01} _{-21.69}	6.67	-0.61 ^{0.08} _{-0.08}	195.66 ^{24.90} _{-26.04}	13.59 ^{9.49} _{-9.37}	6.64	429.79	358.92	-70.87
4.001	4.437	-0.58 ^{0.09} _{-0.09}	124.92 ^{14.48} _{-14.29}	3.56	-0.60 ^{0.10} _{-0.09}	132.87 ^{16.02} _{-20.00}	13.35 ^{8.86} _{-8.84}	3.53	695.6	572.61	-122.99
4.437	5.108	-1.08 ^{0.12} _{-0.12}	130.26 ^{29.84} _{-30.30}	1.24	-1.15 ^{0.16} _{-0.17}	163.67 ^{62.53} _{-55.89}	13.57 ^{5.84} _{-7.45}	1.19	1111.53	1046.04	-65.49
5.108	5.658	-0.51 ^{0.06} _{-0.06}	176.42 ^{15.19} _{-14.84}	7.2	-0.51 ^{0.06} _{-0.06}	176.79 ^{14.66} _{-14.56}	11.70 ^{8.12} _{-8.02}	7.19	876.42	469.15	-407.27
5.658	5.817	-1.08 ^{0.13} _{-0.12}	195.06 ^{53.49} _{-54.56}	2.52	-1.08 ^{0.13} _{-0.13}	197.35 ^{56.99} _{-53.76}	12.38 ^{8.72} _{-8.41}	2.49	-443.23	-734.86	-291.63
5.817	6.178	-1.02 ^{0.14} _{-0.14}	138.89 ^{35.27} _{-35.52}	1.52	-1.05 ^{0.14} _{-0.14}	147.37 ^{36.77} _{-38.45}	12.71 ^{8.09} _{-7.98}	1.51	420.02	387.61	-32.41
15.519	15.668	-0.63 ^{0.09} _{-0.09}	354.56 ^{58.18} _{-57.53}	7.81	-0.55 ^{0.15} _{-0.14}	341.39 ^{55.32} _{-55.45}	12.05 ^{5.04} _{-6.20}	7.6	-345.49	-387.98	-42.49
15.668	15.843	-0.58 ^{0.07} _{-0.07}	243.12 ^{28.50} _{-29.15}	10.7	-0.56 ^{0.09} _{-0.08}	259.37 ^{39.32} _{-38.19}	16.96 ^{7.28} _{-9.40}	10.5	-77.28	-453.35	-376.07
15.843	16.183	-0.59 ^{0.05} _{-0.05}	137.51 ^{10.29} _{-10.36}	9.07	-0.78 ^{0.10} _{-0.10}	222.04 ^{40.16} _{-38.60}	22.40 ^{2.34} _{-2.27}	8.3	648.7	623.03	-25.67
16.183	16.514	-0.81 ^{0.07} _{-0.07}	118.90 ^{12.44} _{-12.21}	5.71	-0.96 ^{0.12} _{-0.12}	189.66 ^{41.37} _{-41.56}	16.37 ^{2.17} _{-2.18}	5.27	486.8	453.18	-33.62
16.514	16.764	-0.90 ^{0.11} _{-0.11}	97.48 ^{15.07} _{-15.47}	3.23	-0.97 ^{0.16} _{-0.15}	114.25 ^{22.70} _{-30.37}	13.08 ^{7.78} _{-8.29}	3.19	123.58	50.2	-73.38
16.764	17.276	-1.08 ^{0.12} _{-0.11}	108.36 ^{22.13} _{-22.37}	1.76	-1.16 ^{0.15} _{-0.17}	141.29 ^{53.87} _{-46.42}	12.34 ^{4.91} _{-5.85}	1.71	837.78	806.21	-31.57
17.276	17.778	-1.13 ^{0.17} _{-0.17}	94.34 ^{26.20} _{-25.86}	1.01	-1.15 ^{0.16} _{-0.16}	99.28 ^{27.17} _{-27.73}	10.97 ^{7.20} _{-6.70}	1.0	721.71	680.42	-41.29

Table B6. Similar to B3 but for GRB 160802A.

T_{start} (s)	T_{stop} (s)	α_{pt}	β_{pt}	E_p (keV)	Flux $\times 10^{-06}$	α_{pt}	β_{pt}	E_p (keV)	kT (keV)	Flux $\times 10^{-06}$	DIC _{Band}	DIC _{Band+BB}	Δ DIC
0.238	0.962	-0.35 ^{0.03} _{-0.04}	-3.05 ^{0.22} _{-0.22}	482.34 ^{19.03} _{-18.64}	24.5	-0.35 ^{0.04} _{-0.04}	-3.09 ^{0.23} _{-0.22}	484.82 ^{19.65} _{-19.31}	12.79 ^{8.40} _{-8.44}	24.3	1547.48	1520.39	-27.09
0.962	1.171	-0.06 ^{0.07} _{-0.07}	-2.53 ^{0.14} _{-0.14}	322.74 ^{19.62} _{-19.73}	35.4	-0.05 ^{0.07} _{-0.08}	-2.54 ^{0.14} _{-0.14}	324.63 ^{18.45} _{-18.48}	12.45 ^{7.42} _{-7.72}	35.4	271.48	258.1	-13.38
1.171	1.695	-0.24 ^{0.04} _{-0.04}	-2.98 ^{0.21} _{-0.21}	337.61 ^{13.48} _{-13.44}	24.1	-0.22 ^{0.06} _{-0.05}	-3.14 ^{0.24} _{-0.24}	367.64 ^{25.85} _{-26.02}	22.64 ^{6.00} _{-6.57}	23.0	1210.93	1194.12	-16.81
1.695	2.16	-0.20 ^{0.06} _{-0.06}	-2.93 ^{0.21} _{-0.21}	244.21 ^{10.86} _{-10.98}	14.3	-0.19 ^{0.06} _{-0.06}	-2.94 ^{0.21} _{-0.21}	244.74 ^{10.94} _{-11.06}	11.44 ^{7.86} _{-7.51}	14.3	957.81	934.19	-23.62
2.16	2.504	-0.26 ^{0.08} _{-0.08}	-2.84 ^{0.24} _{-0.24}	218.85 ^{13.06} _{-13.02}	10.5	-0.26 ^{0.08} _{-0.08}	-2.87 ^{0.25} _{-0.25}	221.21 ^{12.79} _{-13.11}	12.02 ^{7.44} _{-7.44}	10.5	621.01	609.89	-11.12
2.504	3.065	-0.41 ^{0.08} _{-0.08}	-2.81 ^{0.23} _{-0.23}	188.82 ^{12.36} _{-12.52}	6.77	-0.42 ^{0.08} _{-0.08}	-2.85 ^{0.25} _{-0.25}	191.20 ^{12.56} _{-13.23}	12.08 ^{8.42} _{-8.24}	6.73	1104.57	1072.86	-31.71
3.065	3.695	-0.53 ^{0.11} _{-0.11}	-2.78 ^{0.30} _{-0.30}	154.50 ^{14.08} _{-14.00}	3.45	-0.55 ^{0.12} _{-0.11}	-2.84 ^{0.32} _{-0.31}	162.41 ^{14.91} _{-18.11}	12.81 ^{8.08} _{-8.40}	3.48	1100.58	1062.42	-38.16
3.695	4.001	-0.53 ^{0.09} _{-0.09}	-2.69 ^{0.27} _{-0.25}	234.40 ^{21.01} _{-21.23}	8.42	-0.53 ^{0.09} _{-0.09}	-2.73 ^{0.27} _{-0.27}	237.42 ^{21.65} _{-21.59}	12.03 ^{8.35} _{-7.99}	8.3	429.71	401.54	-28.17
4.001	4.437	-0.49 ^{0.10} _{-0.10}	-2.84 ^{0.27} _{-0.26}	160.43 ^{12.15} _{-12.45}	4.27	-0.51 ^{0.11} _{-0.11}	-2.90 ^{0.29} _{-0.29}	165.55 ^{14.25} _{-15.65}	12.48 ^{8.71} _{-8.45}	4.18	698.78	675.55	-23.23
4.437	5.108	-0.90 ^{0.17} _{-0.17}	-2.53 ^{0.24} _{-0.24}	94.46 ^{13.20} _{-13.53}	1.65	-0.97 ^{0.20} _{-0.21}	-2.53 ^{0.26} _{-0.27}	105.02 ^{17.52} _{-22.09}	12.05 ^{6.88} _{-7.51}	1.61	1108.75	1066.05	-42.7
5.108	5.658	-0.48 ^{0.06} _{-0.06}	-3.07 ^{0.27} _{-0.27}	247.67 ^{14.28} _{-14.65}	8.22	-0.48 ^{0.07} _{-0.06}	-3.11 ^{0.29} _{-0.28}	249.03 ^{14.35} _{-14.13}	11.58 ^{7.33} _{-7.43}	8.14	880.39	858.26	-22.13
5.658	5.817	-1.00 ^{0.18} _{-0.19}	-2.66 ^{0.30} _{-0.30}	154.55 ^{37.32} _{-34.20}	3.1	-1.01 ^{0.17} _{-0.18}	-2.73 ^{0.33} _{-0.31}	161.43 ^{36.24} _{-36.02}	12.36 ^{8.12} _{-7.83}	3.0	-442.9	-470.89	-27.99
5.817	6.178	-0.93 ^{0.18} _{-0.18}	-2.66 ^{0.30} _{-0.31}	117.75 ^{19.17} _{-19.55}	1.91	-0.97 ^{0.19} _{-0.18}	-2.70 ^{0.30} _{-0.31}	124.14 ^{19.69} _{-21.99}	12.31 ^{7.92} _{-7.64}	1.85	423.36	405.53	-17.83
15.519	15.668	-0.55 ^{0.11} _{-0.10}	-2.50 ^{0.29} _{-0.28}	390.96 ^{53.51} _{-52.24}	10.5	-0.45 ^{0.18} _{-0.18}	-2.54 ^{0.29} _{-0.28}	387.72 ^{48.19} _{-47.92}	11.64 ^{5.17} _{-6.18}	10.2	-341.25	-350.64	-9.39
15.668	15.843	-0.49 ^{0.10} _{-0.10}	-2.56 ^{0.27} _{-0.25}	291.38 ^{31.89} _{-31.48}	14.3	-0.49 ^{0.09} _{-0.09}	-2.58 ^{0.26} _{-0.26}	302.11 ^{34.42} _{-35.23}	14.09 ^{7.83} _{-7.99}	14.1	-77.42	-87.94	-10.52
15.843	16.183	-0.40 ^{0.09} _{-0.09}	-2.53 ^{0.15} _{-0.15}	155.64 ^{11.95} _{-11.96}	12.2	-0.48 ^{0.14} _{-0.17}	-2.61 ^{0.22} _{-0.22}	175.65 ^{27.72} _{-27.72}	14.64 ^{8.01} _{-9.38}	12.0	634.94	597.83	-37.11
16.183	16.514	-0.54 ^{0.11} _{-0.11}	-2.56 ^{0.14} _{-0.14}	108.64 ^{8.51} _{-8.60}	7.31	-0.63 ^{0.17} _{-0.19}	-2.65 ^{0.21} _{-0.20}	125.48 ^{30.06} _{-22.53}	12.75 ^{5.70} _{-7.05}	7.35	475.27	422.02	-53.25
16.514	16.764	-0.79 ^{0.13} _{-0.13}	-2.75 ^{0.24} _{-0.24}	93.91 ^{8.45} _{-8.80}	3.94	-0.84 ^{0.16} _{-0.14}	-2.74 ^{0.25} _{-0.25}	97.30 ^{8.52} _{-10.50}	12.86 ^{8.33} _{-8.16}	3.87	122.16	99.91	-22.25
16.764	17.276	-0.85 ^{0.17} _{-0.17}	-2.55 ^{0.21} _{-0.20}	78.44 ^{9.09} _{-9.46}	2.3	-0.88 ^{0.16} _{-0.17}	-2.55 ^{0.20} _{-0.20}	80.81 ^{9.00} _{-10.54}	11.32 ^{7.21} _{-7.17}	2.29	829.06	799.69	-29.37
17.276	17.778	-0.97 ^{0.21} _{-0.21}	-2.70 ^{0.28} _{-0.28}	68.69 ^{9.08} _{-9.80}	1.23	-1.01 ^{0.19} _{-0.19}	-2.74 ^{0.28} _{-0.27}	71.10 ^{9.21} _{-9.92}	11.23 ^{7.05} _{-6.91}	1.19	721.85	693.99	-27.86

Table B7. Similar to B4 but for GRB 160802A.

T _{start} (s)	T _{stop} (s)	Synchrotron				DIC	ΔDIC
		B (G)	<i>p</i>	$\gamma_{cool} \times 10^4$ (keV)	Flux ($\times 10^{-06}$)		
0.238	0.962	4.18 ^{0.26} _{-0.25}	5.83 ^{0.13} _{-0.15}	1194.47 ^{1399.32} _{-1060.91}	28.9	567.17	953.22
0.962	1.171	3.44 ^{0.26} _{-0.25}	5.67 ^{0.26} _{-0.28}	1144.14 ^{733.54} _{-1023.01}	36.4	172.61	85.49
1.171	1.695	2.97 ^{0.15} _{-0.15}	5.86 ^{0.11} _{-0.11}	678.58 ^{158.49} _{-533.58}	27.3	1184.84	9.28
1.695	2.16	2.06 ^{0.12} _{-0.12}	5.81 ^{0.15} _{-0.16}	560.14 ^{342.60} _{-424.78}	15.6	1018.2	-84.01
2.16	2.504	1.73 ^{0.14} _{-0.14}	5.64 ^{0.28} _{-0.29}	1620.00 ^{964.20} _{-1505.19}	10.9	314.9	294.99
2.504	3.065	1.36 ^{0.12} _{-0.12}	5.64 ^{0.29} _{-0.31}	869.15 ^{348.88} _{-781.19}	6.7	989.67	83.19
3.065	3.695	1.03 ^{0.14} _{-0.13}	5.35 ^{0.48} _{-0.50}	389.69 ^{305.09} _{-332.53}	3.32	1089.64	-27.22
3.695	4.001	1.60 ^{0.22} _{-0.22}	5.18 ^{0.55} _{-0.58}	764.90 ^{250.38} _{-705.58}	8.14	290.14	111.40
4.001	4.437	1.06 ^{0.13} _{-0.13}	5.40 ^{0.44} _{-0.46}	1122.05 ^{302.24} _{-1053.35}	4.22	564.43	111.12
4.437	5.108	0.42 ^{0.10} _{-0.10}	4.17 ^{0.69} _{-0.67}	771.09 ^{398.85} _{-733.85}	1.49	1071.09	-5.04
5.108	5.658	1.73 ^{0.16} _{-0.16}	5.60 ^{0.31} _{-0.33}	508.68 ^{320.87} _{-424.55}	8.73	851.63	6.63
5.658	5.817	0.63 ^{0.16} _{-0.15}	4.40 ^{0.83} _{-0.79}	719.15 ^{540.68} _{-684.68}	2.79	-462.62	-8.27
5.817	6.178	0.54 ^{0.13} _{-0.13}	4.58 ^{0.86} _{-0.82}	575.98 ^{399.48} _{-541.30}	1.72	402.22	3.31
15.519	15.668	3.17 ^{0.76} _{-0.70}	4.71 ^{0.81} _{-0.78}	547.18 ^{277.70} _{-511.72}	10.6	-385.02	34.38
15.668	15.843	2.13 ^{0.34} _{-0.32}	5.01 ^{0.64} _{-0.66}	862.39 ^{327.78} _{-803.68}	13.5	-146.55	58.61
15.843	16.183	1.14 ^{0.11} _{-0.10}	5.51 ^{0.37} _{-0.39}	569.38 ^{323.31} _{-481.30}	10.5	590.51	7.32
16.183	16.514	0.71 ^{0.11} _{-0.10}	5.14 ^{0.53} _{-0.51}	1061.20 ^{83.48} _{-1009.70}	6.37	61.91	360.11
16.514	16.764	0.49 ^{0.09} _{-0.09}	4.88 ^{0.65} _{-0.65}	585.31 ^{367.03} _{-539.83}	3.67	78.5	21.41
16.764	17.276	0.36 ^{0.08} _{-0.07}	4.22 ^{0.58} _{-0.57}	874.48 ^{412.82} _{-836.44}	2.11	727.01	72.68
17.276	17.778	0.32 ^{0.08} _{-0.08}	4.49 ^{0.77} _{-0.73}	474.60 ^{307.85} _{-441.55}	1.14	715.31	-21.32

Table B8. Similar to B2 but for GRB 160821A.

T _{start} (s)	T _{stop} (s)	CPL			CPL+BB				CPL CPL+BB		
		Γ	E _c (keV)	Flux × 10 ⁻⁰⁶	Γ	E _c (keV)	kT (keV)	Flux × 10 ⁻⁰⁶	DIC	DIC	ΔDIC
113.502	116.61	-1.08 ^{0.04} _{-0.04}	413.39 ^{48.83} _{-49.64}	1.42	-1.13 ^{0.03} _{-0.04}	519.49 ^{104.58} _{-36.26}	12.57 ^{6.89} _{-8.26}	1.63	2985.64	2699.94	-285.7
116.61	117.57	-1.08 ^{0.03} _{-0.03}	565.55 ^{58.97} _{-59.82}	2.98	-1.13 ^{0.23} _{-0.02}	733.21 ^{-2.58} _{-158.28}	13.48 ^{-4.28} _{-7.60}	3.42	1820.7	1741.92	-78.78
117.57	118.04	-1.04 ^{0.04} _{-0.04}	556.07 ^{63.98} _{-61.96}	3.97	-1.07 ^{0.19} _{-0.02}	769.92 ^{34.55} _{-117.99}	2.46 ^{5.21} _{-1.26}	5.3	1097.2	941.09	-156.11
118.04	121.932	-0.99 ^{0.01} _{-0.01}	1013.94 ^{7.01} _{-9.80}	9.47	-0.87 ^{0.02} _{-0.01}	1103.65 ^{0.30} _{-65.64}	11.02 ^{0.50} _{-0.30}	10.9	3555.41	3504.48	-50.93
121.932	124.931	-0.92 ^{0.01} _{-0.01}	996.76 ^{24.19} _{-23.64}	13.9	-0.93 ^{0.02} _{-0.00}	1108.74 ^{-4.65} _{-79.31}	4.79 ^{18.21} _{-0.40}	14.6	3297.32	3265.54	-31.78
124.931	126.547	-0.88 ^{0.01} _{-0.01}	727.63 ^{21.87} _{-23.02}	14.1	-0.92 ^{0.02} _{-0.01}	878.00 ^{31.17} _{-56.76}	7.01 ^{12.59} _{-2.12}	15.2	2624.97	2548.75	-76.22
126.547	127.841	-0.90 ^{0.01} _{-0.01}	634.99 ^{30.29} _{-30.43}	13.9	-0.93 ^{0.02} _{-0.02}	704.33 ^{102.84} _{-10.84}	7.32 ^{21.02} _{-2.02}	14.7	2347.84	2302.58	-45.26
127.841	128.585	-0.85 ^{0.02} _{-0.02}	642.81 ^{39.91} _{-40.26}	17.3	-0.88 ^{0.02} _{-0.02}	742.93 ^{34.86} _{-57.03}	11.82 ^{9.02} _{-7.33}	18.6	1796.85	1632.46	-164.39
128.585	129.887	-0.90 ^{0.01} _{-0.01}	833.84 ^{32.17} _{-31.81}	24.6	-0.93 ^{0.03} _{-0.00}	962.44 ^{17.60} _{-62.79}	8.98 ^{15.62} _{-1.26}	26.1	2566.47	2534.67	-31.8
129.887	131.872	-0.90 ^{0.01} _{-0.01}	1019.74 ^{1.22} _{-2.22}	34.1	-0.91 ^{0.00} _{-0.00}	1168.79 ^{40.02} _{-9.29}	9.27 ^{2.53} _{-1.51}	37.6	3329.64	3274.21	-55.43
131.872	133.589	-0.90 ^{0.01} _{-0.01}	987.29 ^{16.85} _{-17.84}	36.1	-0.93 ^{0.01} _{-0.00}	1265.36 ^{-35.97} _{-90.59}	32.84 ^{0.87} _{-3.59}	38.6	3075.63	3028.8	-46.83
133.589	134.148	-0.89 ^{0.01} _{-0.01}	987.70 ^{33.26} _{-30.61}	41.8	-0.91 ^{0.02} _{-0.00}	1099.90 ^{20.81} _{-66.39}	9.71 ^{11.19} _{-5.78}	44.0	1823.27	1780.98	-42.29
134.148	134.59	-0.84 ^{0.01} _{-0.01}	861.93 ^{28.29} _{-26.73}	44.8	-0.90 ^{0.01} _{-0.01}	1045.02 ^{26.31} _{-62.92}	9.29 ^{13.60} _{-1.68}	49.1	1691.96	1626.66	-65.3
134.59	135.71	-0.84 ^{0.00} _{-0.00}	926.27 ^{10.12} _{-10.15}	56.0	-0.89 ^{0.00} _{-0.00}	1222.16 ^{-0.37} _{-12.92}	26.77 ^{1.05} _{-2.66}	61.4	3164.45	2960.33	-204.12
135.71	135.873	-0.84 ^{0.01} _{-0.01}	1003.58 ^{17.38} _{-17.36}	73.2	-0.88 ^{0.12} _{-0.05}	1259.01 ^{-20.76} _{-108.90}	14.71 ^{4.62} _{-1.42}	84.5	809.16	810.56	1.4
135.873	137.028	-0.86 ^{0.00} _{-0.01}	1020.92 ^{0.04} _{-0.04}	65.9	-0.91 ^{0.00} _{-0.00}	1312.59 ^{0.00} _{-0.00}	19.01 ^{-0.03} _{-0.28}	75.9	3590.86	3288.77	-302.09
137.028	137.967	-0.88 ^{0.00} _{-0.00}	1003.97 ^{16.99} _{-17.75}	51.8	-0.89 ^{0.00} _{-0.00}	1188.07 ^{-4.28} _{-56.93}	24.32 ^{2.04} _{-1.75}	54.9	2538.72	2476.28	-62.44
137.967	139.256	-0.84 ^{0.00} _{-0.00}	893.70 ^{15.55} _{-14.09}	54.7	-0.88 ^{0.01} _{-0.00}	1116.25 ^{-17.64} _{-59.49}	22.38 ^{2.74} _{-1.60}	58.6	2951.09	2855.44	-95.65
139.256	139.514	-0.84 ^{0.02} _{-0.02}	705.85 ^{45.15} _{-44.93}	39.1	-0.88 ^{0.03} _{-0.02}	805.88 ^{45.74} _{-59.27}	10.22 ^{10.50} _{-5.30}	41.5	885.19	803.07	-82.12
139.514	141.152	-0.88 ^{0.00} _{-0.00}	746.89 ^{14.64} _{-14.80}	33.1	-0.91 ^{0.01} _{-0.01}	828.39 ^{86.64} _{-23.62}	7.21 ^{21.29} _{-14.16}	35.1	2918.39	2875.22	-43.17
141.152	142.733	-0.89 ^{0.01} _{-0.01}	727.48 ^{25.31} _{-24.21}	25.2	-0.91 ^{0.01} _{-0.01}	777.04 ^{41.98} _{-21.86}	9.81 ^{14.30} _{-3.95}	26.1	2720.91	2669.02	-51.89
142.733	143.378	-0.98 ^{0.02} _{-0.02}	497.66 ^{35.79} _{-35.84}	11.3	-1.01 ^{0.05} _{-0.02}	560.59 ^{72.04} _{-34.04}	7.42 ^{14.11} _{-1.88}	11.9	1493.9	1464.38	-29.52
143.378	145.559	-1.05 ^{0.01} _{-0.01}	585.29 ^{26.93} _{-27.34}	9.72	-1.07 ^{0.02} _{-0.01}	638.50 ^{53.72} _{-25.54}	12.29 ^{8.30} _{-4.61}	10.1	2865.0	2804.88	-60.12
145.559	145.673	-0.77 ^{0.03} _{-0.03}	702.76 ^{54.08} _{-55.45}	32.6	-0.81 ^{0.07} _{-0.02}	800.63 ^{56.90} _{-75.84}	16.56 ^{0.72} _{-11.85}	35.0	-59.7	-128.93	-69.23
145.673	145.769	-0.79 ^{0.03} _{-0.03}	708.21 ^{54.71} _{-54.77}	46.0	-0.85 ^{0.08} _{-0.00}	871.42 ^{16.73} _{-110.63}	9.30 ^{11.21} _{-3.10}	50.4	-151.59	-201.94	-50.35
145.769	145.897	-0.96 ^{0.04} _{-0.04}	488.42 ^{52.47} _{-51.57}	16.5	-1.03 ^{0.05} _{-0.02}	688.89 ^{51.64} _{-85.03}	10.53 ^{10.27} _{-5.13}	19.6	-76.55	-120.96	-44.41
145.897	146.391	-1.07 ^{0.03} _{-0.03}	441.26 ^{37.92} _{-38.65}	8.61	-1.12 ^{0.04} _{-0.02}	512.53 ^{49.42} _{-51.32}	11.99 ^{7.57} _{-7.85}	9.05	1145.66	1059.59	-86.07
146.391	146.983	-1.10 ^{0.03} _{-0.03}	473.11 ^{45.39} _{-45.17}	7.56	-1.14 ^{0.01} _{-0.04}	570.21 ^{98.02} _{-19.27}	9.84 ^{9.93} _{-5.56}	8.55	1411.7	1257.49	-154.21
146.983	148.176	-1.10 ^{0.02} _{-0.02}	589.39 ^{43.09} _{-42.28}	7.15	-1.13 ^{0.03} _{-0.01}	704.62 ^{39.70} _{-68.83}	13.89 ^{6.22} _{-8.87}	7.65	2116.82	2073.09	-43.73
148.176	148.711	-1.01 ^{0.03} _{-0.03}	585.42 ^{48.33} _{-49.21}	10.2	-1.05 ^{0.05} _{-0.01}	698.27 ^{57.19} _{-61.93}	9.41 ^{11.43} _{-2.68}	11.0	1279.5	1214.63	-64.87
148.711	150.562	-1.09 ^{0.02} _{-0.02}	595.76 ^{34.81} _{-34.51}	8.04	-1.12 ^{0.05} _{-0.01}	674.29 ^{30.80} _{-60.02}	13.73 ^{3.53} _{-7.17}	8.41	2616.63	2570.55	-46.08
150.562	152.277	-1.12 ^{0.02} _{-0.02}	600.65 ^{41.44} _{-41.06}	6.07	-1.15 ^{0.05} _{-0.01}	700.04 ^{39.91} _{-71.90}	13.21 ^{4.11} _{-7.69}	6.43	2438.16	2393.85	-44.31
152.277	153.139	-1.11 ^{0.03} _{-0.03}	514.96 ^{52.51} _{-52.70}	4.35	-1.15 ^{0.02} _{-0.03}	642.16 ^{96.29} _{-36.55}	15.66 ^{3.75} _{-11.66}	4.94	1700.95	1224.97	-475.98
153.139	154.931	-1.07 ^{0.03} _{-0.03}	459.31 ^{39.60} _{-39.76}	3.5	-1.12 ^{0.04} _{-0.02}	586.86 ^{30.06} _{-81.18}	7.30 ^{13.21} _{-2.72}	3.78	2440.88	2304.6	-136.28
154.931	157.145	-1.12 ^{0.03} _{-0.03}	449.95 ^{48.84} _{-48.66}	2.27	-1.16 ^{0.03} _{-0.03}	567.71 ^{70.22} _{-56.92}	6.10 ^{14.39} _{-0.23}	2.48	2586.5	2547.01	-39.49
157.145	160.646	-1.17 ^{0.03} _{-0.03}	432.00 ^{50.17} _{-50.70}	1.48	-1.22 ^{0.03} _{-0.03}	542.85 ^{96.77} _{-45.27}	11.34 ^{8.34} _{-7.26}	1.65	2981.17	2897.26	-83.91
160.646	164.983	-1.12 ^{0.05} _{-0.05}	374.31 ^{51.70} _{-50.77}	0.9	-1.19 ^{0.04} _{-0.04}	480.73 ^{113.28} _{-39.45}	13.98 ^{5.58} _{-9.87}	1.02	3201.59	3148.64	-52.95
164.983	177.789	-1.08 ^{0.05} _{-0.05}	344.63 ^{50.23} _{-49.70}	0.56	-1.14 ^{0.03} _{-0.06}	456.29 ^{94.81} _{-42.13}	15.76 ^{3.80} _{-11.13}	0.63	4275.35	4210.26	-65.09

Table B9. Similar to B3 but for GRB 160821A.

T_{start} (s)	T_{stop} (s)	α_{pt}	β_{pt}	E_{p} (keV)	Flux $\times 10^{-06}$	α_{pt}	β_{pt}	E_{p} (keV)	kT (keV)	Flux $\times 10^{-06}$	DIC _{Band}	DIC _{Band+BB}	Δ DIC
113.502	116.61	-1.09 ^{0.05} _{-0.05}	-2.47 ^{-0.33} _{-0.34}	363.47 ^{50.31} _{-50.12}	2.01	-1.09 ^{0.05} _{-0.05}	-2.53 ^{0.34} _{-0.34}	369.79 ^{48.92} _{-48.55}	10.53 ^{7.42} _{-7.03}	1.93	2982.03	2891.22	-90.81
116.61	117.57	-1.12 ^{0.04} _{-0.04}	-2.63 ^{-0.32} _{-0.32}	534.22 ^{58.48} _{-58.89}	3.81	-1.03 ^{0.14} _{-0.11}	-2.62 ^{0.33} _{-0.33}	507.26 ^{60.33} _{-59.38}	8.80 ^{5.17} _{-3.74}	3.82	1814.18	1765.9	-48.28
117.57	118.04	-1.07 ^{0.05} _{-0.05}	-2.31 ^{-0.28} _{-0.29}	498.24 ^{70.42} _{-70.21}	5.97	-1.01 ^{0.11} _{-0.09}	-2.36 ^{0.31} _{-0.32}	493.90 ^{75.00} _{-73.68}	8.62 ^{6.31} _{-4.94}	5.87	1090.81	783.94	-306.87
118.04	121.932	-0.97 ^{0.01} _{-0.01}	-1.93 ^{-0.03} _{-0.03}	758.51 ^{19.61} _{-19.71}	17.8	-0.82 ^{0.03} _{-0.03}	-1.92 ^{0.03} _{-0.02}	701.64 ^{24.98} _{-26.73}	8.85 ^{0.55} _{-0.60}	18.3	3490.81	3470.81	-20.0
121.932	124.931	-0.85 ^{0.01} _{-0.01}	-2.08 ^{-0.03} _{-0.04}	736.18 ^{17.92} _{-16.51}	21.1	-0.84 ^{0.03} _{-0.03}	-2.14 ^{-0.05} _{-0.05}	807.42 ^{29.42} _{-30.73}	7.88 ^{1.86} _{-2.53}	20.8	3270.87	3242.14	-28.73
124.931	126.547	-0.81 ^{0.01} _{-0.01}	-2.36 ^{-0.02} _{-0.03}	632.87 ^{12.04} _{-12.32}	18.4	-0.87 ^{0.01} _{-0.01}	-2.32 ^{0.08} _{-0.08}	717.15 ^{22.88} _{-22.08}	9.52 ^{4.13} _{-4.98}	19.9	2634.44	2603.95	-30.49
126.547	127.841	-0.89 ^{0.02} _{-0.02}	-2.60 ^{-0.16} _{-0.16}	646.56 ^{34.52} _{-34.10}	17.4	-0.88 ^{0.02} _{-0.02}	-2.58 ^{-0.15} _{-0.14}	636.62 ^{32.01} _{-32.28}	11.91 ^{7.39} _{-7.12}	17.3	2336.9	2324.75	-12.15
127.841	128.585	-0.81 ^{0.02} _{-0.02}	-2.28 ^{-0.10} _{-0.10}	616.41 ^{35.00} _{-36.40}	25.4	-0.78 ^{0.04} _{-0.04}	-2.26 ^{0.08} _{-0.08}	597.52 ^{37.35} _{-37.26}	8.94 ^{5.58} _{-4.73}	25.7	1773.68	1742.53	-31.15
128.585	129.887	-0.84 ^{0.01} _{-0.01}	-2.14 ^{-0.05} _{-0.05}	686.91 ^{19.72} _{-19.30}	37.8	-0.85 ^{0.01} _{-0.02}	-2.17 ^{-0.05} _{-0.05}	713.85 ^{30.36} _{-30.36}	12.41 ^{6.68} _{-6.58}	37.3	2473.34	2458.33	-15.01
129.887	131.872	-0.83 ^{0.01} _{-0.01}	-2.09 ^{-0.02} _{-0.02}	780.83 ^{10.11} _{-10.46}	51.9	-0.81 ^{0.01} _{-0.01}	-2.04 ^{-0.01} _{-0.01}	732.84 ^{11.80} _{-11.10}	15.06 ^{1.85} _{-1.47}	53.7	3133.25	3131.92	-1.33
131.872	133.589	-0.78 ^{0.00} _{-0.00}	-2.18 ^{-0.02} _{-0.02}	692.47 ^{8.88} _{-8.27}	49.0	-0.82 ^{0.01} _{-0.01}	-2.14 ^{-0.02} _{-0.02}	747.37 ^{13.40} _{-12.99}	13.60 ^{4.87} _{-5.24}	52.0	2969.33	2927.3	-42.03
133.589	134.148	-0.79 ^{0.02} _{-0.02}	-2.00 ^{-0.04} _{-0.04}	710.41 ^{38.04} _{-37.21}	69.3	-0.62 ^{0.07} _{-0.07}	-1.97 ^{0.03} _{-0.03}	608.89 ^{34.76} _{-34.22}	9.26 ^{0.89} _{-1.12}	70.5	1679.12	1673.73	-5.39
134.148	134.59	-0.76 ^{0.02} _{-0.02}	-1.96 ^{-0.04} _{-0.04}	659.52 ^{36.70} _{-35.75}	80.2	-0.75 ^{0.02} _{-0.03}	-1.96 ^{-0.04} _{-0.04}	648.69 ^{35.26} _{-36.09}	12.65 ^{6.72} _{-6.72}	80.1	1499.1	1489.29	-9.81
134.59	135.71	-0.75 ^{0.00} _{-0.00}	-1.97 ^{-0.01} _{-0.01}	683.93 ^{12.74} _{-10.92}	95.2	-0.79 ^{0.01} _{-0.01}	-1.97 ^{-0.01} _{-0.02}	735.11 ^{12.87} _{-12.12}	13.94 ^{3.85} _{-3.66}	95.7	2661.89	2623.38	-38.51
135.71	135.873	-0.73 ^{0.03} _{-0.03}	-1.75 ^{-0.04} _{-0.04}	611.61 ^{54.97} _{-53.96}	163.4	-0.68 ^{0.05} _{-0.05}	-1.74 ^{-0.03} _{-0.03}	561.89 ^{52.07} _{-52.06}	10.16 ^{6.32} _{-5.51}	167.0	594.0	580.8	-13.2
135.873	137.028	-0.82 ^{0.01} _{-0.01}	-1.88 ^{-0.01} _{-0.01}	794.60 ^{9.98} _{-9.37}	127.94	-0.75 ^{0.02} _{-0.02}	-1.87 ^{-0.01} _{-0.01}	734.44 ^{18.16} _{-13.35}	7.15 ^{0.60} _{-0.66}	129.7	2665.56	2656.52	-9.04
137.028	137.967	-0.79 ^{0.01} _{-0.01}	-2.07 ^{-0.03} _{-0.03}	697.71 ^{8.27} _{-8.75}	76.5	-0.81 ^{0.01} _{-0.01}	-2.13 ^{-0.03} _{-0.03}	760.55 ^{17.10} _{-17.18}	7.77 ^{3.68} _{-4.06}	74.0	2396.85	2364.43	-32.42
137.967	139.256	-0.75 ^{0.00} _{-0.00}	-2.15 ^{-0.02} _{-0.02}	696.61 ^{5.21} _{-5.83}	77.9	-0.74 ^{0.03} _{-0.03}	-2.16 ^{-0.01} _{-0.02}	753.38 ^{17.70} _{-17.50}	10.42 ^{0.66} _{-0.67}	79.5	2771.78	2719.58	-52.2
139.256	139.514	-0.79 ^{0.03} _{-0.03}	-2.14 ^{-0.07} _{-0.07}	628.30 ^{42.08} _{-41.27}	62.9	-0.74 ^{0.07} _{-0.06}	-2.12 ^{-0.06} _{-0.06}	599.38 ^{46.11} _{-47.34}	10.06 ^{0.98} _{-5.21}	63.3	821.53	740.32	-81.21
139.514	141.152	-0.87 ^{0.01} _{-0.01}	-2.58 ^{-0.08} _{-0.08}	761.42 ^{24.41} _{-24.53}	40.7	-0.86 ^{0.01} _{-0.01}	-2.54 ^{-0.06} _{-0.06}	742.08 ^{19.74} _{-19.63}	13.53 ^{5.22} _{-5.33}	40.9	2856.76	2847.64	-9.12
141.152	142.733	-0.86 ^{0.01} _{-0.01}	-2.64 ^{-0.10} _{-0.11}	725.05 ^{17.06} _{-16.93}	30.2	-0.85 ^{0.01} _{-0.01}	-2.58 ^{-0.08} _{-0.08}	703.22 ^{17.57} _{-17.61}	12.38 ^{6.26} _{-5.97}	30.5	2706.29	2675.24	-31.05
142.733	143.378	-0.97 ^{0.03} _{-0.03}	-2.61 ^{-0.24} _{-0.24}	467.30 ^{37.87} _{-37.17}	14.0	-0.96 ^{0.04} _{-0.04}	-2.66 ^{-0.25} _{-0.25}	477.88 ^{38.45} _{-38.76}	13.05 ^{6.03} _{-6.93}	13.8	1489.62	1478.37	-11.25
143.378	145.559	-1.05 ^{0.02} _{-0.02}	-2.88 ^{-0.26} _{-0.25}	545.48 ^{26.51} _{-26.31}	11.2	-1.04 ^{0.02} _{-0.02}	-2.91 ^{-0.25} _{-0.26}	549.31 ^{27.21} _{-27.43}	12.70 ^{6.16} _{-6.47}	11.1	2862.41	2851.62	-10.79
145.559	145.673	-0.72 ^{0.05} _{-0.05}	-1.97 ^{-0.08} _{-0.08}	610.46 ^{52.14} _{-54.24}	61.4	-0.62 ^{0.14} _{-0.12}	-2.03 ^{-0.10} _{-0.10}	610.66 ^{68.83} _{-69.49}	8.81 ^{4.01} _{-4.10}	58.1	-67.5	-106.8	-39.3
145.673	145.769	-0.69 ^{0.04} _{-0.05}	-1.99 ^{-0.08} _{-0.08}	562.35 ^{53.39} _{-52.40}	83.0	-0.65 ^{0.07} _{-0.08}	-1.99 ^{-0.07} _{-0.08}	554.74 ^{54.27} _{-54.22}	11.78 ^{5.95} _{-6.25}	83.4	-184.38	-193.79	-9.41
145.769	145.897	-0.89 ^{0.06} _{-0.06}	-1.96 ^{-0.10} _{-0.10}	362.54 ^{53.61} _{-53.29}	35.6	-0.88 ^{0.06} _{-0.06}	-1.96 ^{-0.10} _{-0.10}	362.52 ^{54.08} _{-54.82}	11.32 ^{7.13} _{-7.08}	35.4	-103.91	-117.13	-13.22
145.897	146.391	-1.08 ^{0.03} _{-0.03}	-3.07 ^{-0.28} _{-0.28}	406.54 ^{30.31} _{-30.41}	9.61	-1.08 ^{0.03} _{-0.03}	-3.11 ^{-0.28} _{-0.28}	407.21 ^{30.52} _{-30.84}	10.97 ^{7.49} _{-7.18}	9.51	1145.97	1121.5	-24.47
146.391	146.983	-1.09 ^{0.04} _{-0.04}	-2.26 ^{-0.16} _{-0.15}	371.06 ^{39.67} _{-40.38}	11.8	-1.08 ^{0.04} _{-0.04}	-2.26 ^{-0.16} _{-0.16}	372.61 ^{40.14} _{-39.73}	11.03 ^{7.66} _{-7.18}	11.8	1399.34	1365.12	-34.22
146.983	148.176	-1.09 ^{0.03} _{-0.03}	-2.36 ^{-0.18} _{-0.18}	483.92 ^{46.20} _{-44.87}	10.2	-1.08 ^{0.03} _{-0.03}	-2.36 ^{-0.19} _{-0.19}	483.75 ^{46.97} _{-46.47}	10.77 ^{7.17} _{-6.37}	10.1	2107.17	2087.04	-20.13
148.176	148.711	-0.98 ^{0.04} _{-0.04}	-2.24 ^{-0.19} _{-0.19}	483.08 ^{60.76} _{-61.44}	15.8	-0.98 ^{0.04} _{-0.04}	-2.26 ^{-0.19} _{-0.19}	489.50 ^{58.70} _{-59.09}	11.72 ^{6.92} _{-7.17}	15.5	1271.55	1255.57	-15.98
148.711	150.562	-1.10 ^{0.02} _{-0.02}	-2.89 ^{-0.27} _{-0.28}	538.82 ^{31.24} _{-31.21}	9.24	-1.08 ^{0.03} _{-0.03}	-2.92 ^{-0.28} _{-0.28}	539.46 ^{31.28} _{-31.27}	10.65 ^{4.80} _{-5.12}	9.15	2613.3	2598.72	-14.58
150.562	152.277	-1.13 ^{0.02} _{-0.02}	-2.61 ^{-0.25} _{-0.25}	525.39 ^{40.47} _{-39.39}	7.69	-1.10 ^{0.05} _{-0.04}	-2.62 ^{-0.24} _{-0.25}	519.61 ^{40.34} _{-39.70}	9.66 ^{4.45} _{-4.41}	7.61	2429.94	2407.02	-22.92
152.277	153.139	-1.11 ^{0.04} _{-0.04}	-2.04 ^{-0.13} _{-0.13}	403.33 ^{54.84} _{-54.59}	8.74	-1.08 ^{0.05} _{-0.06}	-2.04 ^{-0.13} _{-0.13}	392.42 ^{55.58} _{-55.22}	9.30 ^{7.67} _{-6.09}	8.66	1684.78	1068.64	-616.14
153.139	154.931	-1.08 ^{0.03} _{-0.03}	-2.87 ^{-0.30} _{-0.30}	425.24 ^{37.22} _{-36.70}	4.13	-1.07 ^{0.03} _{-0.04}	-2.84 ^{-0.30} _{-0.29}	424.83 ^{36.18} _{-35.97}	10.64 ^{6.91} _{-6.40}	4.1	2439.25	2409.62	-29.63
154.931	157.145	-1.10 ^{0.05} _{-0.05}	-2.24 ^{-0.27} _{-0.29}	343.53 ^{63.32} _{-66.54}	3.73	-1.11 ^{0.05} _{-0.05}	-2.30 ^{-0.31} _{-0.31}	358.59 ^{61.57} _{-64.58}	12.06 ^{7.40} _{-7.68}	3.49	2578.76	2526.67	-52.09
157.145	160.646	-1.18 ^{0.05} _{-0.05}	-2.42 ^{-0.30} _{-0.30}	342.97 ^{53.00} _{-51.66}	2.1	-1.18 ^{0.04} _{-0.05}	-2.47 ^{-0.32} _{-0.33}	350.79 ^{50.50} _{-52.08}	11.22 ^{7.65} _{-7.27}	2.03	2975.14	2929.82	-45.32
160.646	164.983	-1.15 ^{0.05} _{-0.05}	-2.54 ^{-0.33} _{-0.34}	337.38 ^{44.93} _{-44.49}	1.22	-1.13 ^{0.06} _{-0.06}	-2.60 ^{-0.33} _{-0.34}	342.65 ^{44.23} _{-43.14}	10.09 ^{6.39} _{-5.97}	1.18	3197.95	3164.91	-33.04
164.983	177.789	-1.09 ^{0.06} _{-0.06}	-2.65 ^{-0.34} _{-0.33}	309.72 ^{40.48} _{-38.87}	0.7	-1.09 ^{0.06} _{-0.06}	-2.71 ^{-0.35} _{-0.33}	315.63 ^{40.02} _{-38.83}	10.26 ^{6.74} _{-6.46}	0.69	4274.2	4231.59	-42.61

Table B10. Similar to B4 but for GRB 160821A.

T _{start} (s)	T _{stop} (s)	Synchrotron				DIC	ΔDIC
		B (G)	p	$\gamma_{cool} \times 10^4$ (keV)	Flux ($\times 10^{-06}$)		
113.502	116.61	0.43 ^{0.08} _{0.08}	2.02 ^{0.29} _{0.29}	20.78 ^{181.07} _{9.11}	3.37	2945.62	-54.40
116.61	117.57	0.20 ^{0.04} _{0.04}	2.00 ^{0.08} _{0.08}	86.02 ^{116.96} _{3.74}	8.93	1797.94	-32.04
117.57	118.04	0.24 ^{0.05} _{0.05}	2.01 ^{0.06} _{0.06}	127.32 ^{247.21} _{5.85}	15.1	1103.45	-319.51
118.04	121.932	0.60 ^{0.06} _{0.06}	2.00 ^{0.03} _{0.03}	56.55 ^{12.66} _{-6.05}	21.0	3549.22	-78.41
121.932	124.931	2.06 ^{0.20} _{0.20}	2.37 ^{0.10} _{0.10}	20.02 ^{6.71} _{0.44}	23.2	3238.28	3.86
124.931	126.547	2.21 ^{0.23} _{0.23}	2.89 ^{0.18} _{0.18}	20.25 ^{5.58} _{0.27}	20.9	2609.42	-5.47
126.547	127.841	1.64 ^{0.24} _{0.24}	2.66 ^{0.15} _{0.15}	20.02 ^{18.79} _{0.95}	21.9	2267.37	57.38
127.841	128.585	2.27 ^{0.40} _{0.40}	3.06 ^{0.26} _{0.26}	20.44 ^{79.31} _{1.84}	25.9	1584.11	158.42
128.585	129.887	2.05 ^{0.23} _{0.23}	2.60 ^{0.11} _{0.11}	20.04 ^{10.70} _{0.65}	38.8	2438.24	20.09
129.887	131.872	2.27 ^{0.14} _{0.14}	2.45 ^{0.07} _{0.07}	20.09 ^{3.41} _{0.19}	54.4	3067.63	64.29
131.872	133.589	2.38 ^{0.15} _{0.15}	2.64 ^{0.08} _{0.08}	20.02 ^{4.20} _{0.29}	53.3	2875.96	51.34
133.589	134.148	2.25 ^{0.34} _{0.34}	2.43 ^{0.13} _{0.13}	20.34 ^{29.79} _{1.41}	68.3	1603.99	69.74
134.148	134.59	2.21 ^{0.33} _{0.33}	2.39 ^{0.17} _{0.17}	20.09 ^{60.77} _{3.27}	79.2	1352.96	136.33
134.59	135.71	2.29 ^{0.23} _{0.23}	2.36 ^{0.06} _{0.06}	20.01 ^{9.20} _{0.49}	94.4	2541.6	81.78
135.71	135.873	1.74 ^{0.22} _{0.22}	2.00 ^{0.18} _{0.18}	25.70 ^{71.34} _{8.01}	161.2	527.94	52.86
135.873	137.028	2.17 ^{0.23} _{0.23}	2.16 ^{0.06} _{0.06}	20.13 ^{11.24} _{0.52}	126.54	2589.97	66.55
137.028	137.967	2.40 ^{0.21} _{0.21}	2.57 ^{0.08} _{0.08}	20.21 ^{6.46} _{0.23}	77.9	2270.0	94.43
137.967	139.256	2.78 ^{0.15} _{0.15}	2.89 ^{0.09} _{0.09}	20.01 ^{2.22} _{0.22}	76.5	2667.54	52.04
139.256	139.514	2.29 ^{0.36} _{0.36}	2.82 ^{0.26} _{0.26}	20.16 ^{177.44} _{4.32}	62.3	718.83	21.49
139.514	141.152	2.34 ^{0.12} _{0.12}	3.13 ^{0.11} _{0.11}	20.05 ^{2.56} _{0.19}	44.1	2842.4	5.24
141.152	142.733	2.42 ^{0.14} _{0.14}	3.40 ^{0.17} _{0.17}	20.05 ^{2.89} _{0.20}	32.1	2713.12	-37.88
142.733	143.378	1.02 ^{0.18} _{0.18}	2.65 ^{0.20} _{0.20}	20.00 ^{37.89} _{1.61}	17.6	1447.06	31.31
143.378	145.559	0.85 ^{0.09} _{0.09}	2.42 ^{0.09} _{0.09}	20.00 ^{9.17} _{0.56}	16.1	2904.37	-52.75
145.559	145.673	3.13 ^{0.61} _{0.61}	2.99 ^{0.43} _{0.43}	20.08 ^{367.29} _{5.37}	52.4	-192.62	85.82
145.673	145.769	2.69 ^{0.47} _{0.47}	2.81 ^{0.34} _{0.34}	21.00 ^{339.00} _{4.44}	76.3	-348.92	155.13
145.769	145.897	0.78 ^{0.12} _{0.12}	2.05 ^{0.37} _{0.37}	20.30 ^{204.60} _{12.76}	38.6	-238.95	121.82
145.897	146.391	0.62 ^{0.11} _{0.11}	2.44 ^{0.20} _{0.20}	20.04 ^{41.06} _{2.24}	14.4	1146.87	-25.37
146.391	146.983	0.44 ^{0.07} _{0.07}	2.04 ^{0.19} _{0.19}	20.82 ^{59.19} _{5.76}	16.5	1367.03	-1.91
146.983	148.176	0.52 ^{0.07} _{0.07}	2.03 ^{0.17} _{0.17}	20.53 ^{45.72} _{7.12}	14.5	2087.4	-0.36
148.176	148.711	0.77 ^{0.13} _{0.13}	2.16 ^{0.19} _{0.19}	20.17 ^{54.84} _{5.23}	19.5	1247.27	8.30
148.711	150.562	0.62 ^{0.10} _{0.10}	2.18 ^{0.10} _{0.10}	20.02 ^{25.35} _{1.78}	15.1	2612.08	-13.36
150.562	152.277	0.30 ^{0.05} _{0.05}	2.05 ^{0.09} _{0.09}	40.90 ^{24.89} _{-5.68}	12.9	2445.17	-38.15
152.277	153.139	0.25 ^{0.04} _{0.04}	2.01 ^{0.13} _{0.13}	48.59 ^{86.18} _{6.23}	11.5	1685.38	-616.74
153.139	154.931	0.57 ^{0.10} _{0.10}	2.24 ^{0.19} _{0.19}	20.63 ^{50.57} _{2.88}	6.84	2384.97	24.65
154.931	157.145	0.39 ^{0.05} _{0.05}	2.01 ^{0.27} _{0.27}	20.73 ^{128.52} _{13.36}	5.14	2526.83	-0.16
157.145	160.646	0.31 ^{0.05} _{0.05}	2.02 ^{0.25} _{0.25}	21.45 ^{105.84} _{13.31}	3.3	2966.7	-36.88
160.646	164.983	0.34 ^{0.06} _{0.06}	2.02 ^{0.31} _{0.31}	20.48 ^{234.69} _{14.47}	2.14	3176.7	-11.79
164.983	177.789	0.44 ^{0.09} _{0.09}	2.24 ^{0.34} _{0.34}	20.17 ^{341.39} _{8.08}	1.14	4239.76	-8.17

Table B11. The Pearson correlation (r) between parameters obtained using time-resolved spectral analysis of GRB 160325A, GRB 160802A, and GRB 160821A, respectively.

GRB 160325A								
Model	$\log(\text{Flux})-\log(E_p)$		$\log(\text{Flux})-\alpha_{\text{pt}}$		$\log(E_p)-\alpha_{\text{pt}}$		$\log(\text{Flux})-kT$	
	r	Probability of null hypothesis (p)	r	p	r	p	r	p
Band	0.70	0.29	-0.90	0.10	-0.72	0.28	-	-
Band+BB	0.75	0.25	-0.93	0.07	-0.56	0.44	-0.31	0.68
$\log(\text{Flux})-\log(B)$			$\log(\text{Flux})-p$			$\log(B)-p$		
	r	p	r	p	r	p	r	p
Synchrotron	-0.22	0.78	-0.77		0.23		0.74	0.26
$\log(E_p)-\log(B)$			$\log(B)-\alpha_{\text{pt}}$			$\alpha_{\text{pt}}-p$		
	r	p	r	p	r	p	r	p
Band+BB-Synchrotron	0.38	0.61		0.55	0.45		0.88	0.12
GRB 160802A								
Model	$\log(\text{Flux})-\log(E_p)$		$\log(\text{Flux})-\alpha_{\text{pt}}$		$\log(E_p)-\alpha_{\text{pt}}$		$\log(\text{Flux})-kT$	
	r	Probability of null hypothesis (p)	r	p	r	p	r	p
Band	0.87	8.21×10^{-7}	0.90	6.85×10^{-8}	0.74	1.95×10^{-4}	-	-
Band+BB	0.87	4.43×10^{-8}	0.91	2.32×10^{-8}	0.80	2.31×10^{-5}	0.40	0.08
$\log(\text{Flux})-\log(B)$			$\log(\text{Flux})-p$			$\log(B)-p$		
	r	p	r	p	r	p	r	p
Synchrotron	0.93	1.51×10^{-9}	0.81		1.66×10^{-5}		0.76	9.85×10^{-5}
$\log(E_p)-\log(B)$			$\log(B)-\alpha_{\text{pt}}$			$\alpha_{\text{pt}}-p$		
	r	p	r	p	r	p	r	p
Band+BB-Synchrotron	0.98	2.72×10^{-14}	0.89		1.24×10^{-7}		0.89	2.01×10^{-7}
GRB 160821A								
Model	$\log(\text{Flux})-\log(E_p)$		$\log(\text{Flux})-\alpha_{\text{pt}}$		$\log(E_p)-\alpha_{\text{pt}}$		$\log(\text{Flux})-kT$	
	r	Probability of null hypothesis (p)	r	p	r	p	r	p
Band	0.79	4.87×10^{-9}	0.90	2.69×10^{-14}	0.74	8.39×10^{-8}	-	-
Band+BB	0.77	1.98×10^{-8}	0.89	1.63×10^{-13}	0.73	2.26×10^{-7}	0.10	0.56
$\log(\text{Flux})-\log(B)$			$\log(\text{Flux})-p$			$\log(B)-p$		
	r	p	r	p	r	p	r	p
Synchrotron	0.79	4.33×10^{-9}	0.43		7.34×10^{-3}		0.76	2.73×10^{-8}
$\log(E_p)-\log(B)$			$\log(B)-\alpha_{\text{pt}}$			$\alpha_{\text{pt}}-p$		
	r	p	r	p	r	p	r	p
Band-Synchrotron	0.77	2.19×10^{-8}	0.94		2.23×10^{-18}		0.63	2.12×10^{-5}